THESIS

CHARACTERISTICS OF LINEAR MESOSCALE CONVECTIVE SYSTEMS DURING DYNAMO

Submitted by

Joseph Messina

Department of Atmospheric Science

In partial fulfillment of the requirements

For the Degree of Master of Science

Colorado State University

Fort Collins, Colorado

Fall 2019

Master's Committee:

Advisor: Steven Rutledge

Weixin Xu
Kristen Rasmussen
Richard Eykholt

ABSTRACT

CHARACTERISTICS OF LINEAR MESOSCALE CONVECTIVE SYSTEMS DURING DYNAMO

Mesoscale convective systems (MCSs) have long been known to play a large part in the vertical transport of horizontal momentum. They also contribute to the vertical redistribution of heat and radiative forcing. The Madden Julian Oscillation (MJO) is a tropical disturbance that propagates across the central Indian Ocean and western Pacific Ocean with an intraseasonal cycle of 30-60 days. Many studies have explored the kinematic characteristics and organization of MCSs in the tropics, while others investigated the characteristics of convective systems within the MJO. However, there remains a gap in current literature on the connection between MJO phase and kinematics of precipitating tropical convection. Those studies that did examine MCSs in the tropical environment did so with limited observations.

This study used radar, sounding, and meteorological data from the Dynamics of the Madden Julian Oscillation (DYNAMO) field campaign in the central Indian Ocean to examine the influence of vertical shear on the orientation of linear MCSs, effects of cold pools on propagation of linear systems, and the mesoscale flow features of the MCSs over the phases of the MJO. DYNAMO took place from October-December 2011 and produced a vast dataset for the analysis of tropical convection during multiple MJO events. Our results show that convection during DYNAMO was consistent with studies from previous tropical field campaigns. That is, convective lines are frequently oriented perpendicular to strong low-level shear. In the absence of strong low-level shear, they are oriented parallel to strong mid-level shear. Linear systems were more prevalent during active MJO phases. Cold pools did not

play a substantial role in tropical squall line propagation. Kinematic features are also consistent with previous works. The presence of a jump updraft and descending rear inflow were ubiquitous in our samples. The absence of a downdraft outflow was common. This result shows that the MCSs studied were transporting front to rear horizontal momentum from low- to mid-levels and rear to front horizontal momentum from low- to mid-levels.

ACKNOWLEDGEMENTS

I would first like to thank Dr. Steven Rutledge, my advisor, for his guidance, motivation, patience, and understanding. His approach to science is an inspiration to never stop asking "why?", and to never be satisfied with a less-than-complete understanding of the physical process you are investigating. I would like to thank Dr. Brenda Dolan for her selfless willingness to answer my endless questions on radar meteorology, Python programming, and the writing process. Thank you also to Paul Hein for his computer support and guidance in data acquisition and computer programming. Paul's expertise will be sorely missed in his retirement. I thank Dr. Weixin Xu for his guidance and expertise in tropical meteorology early in the project, and for participating on my committee. I would also like to thank the rest of my committee— Dr. Kristen Rasmussen and Dr. Richard Eykholt. Thank you to Dr. Leah Grant for answering my questions on her research. Thank you also to Paul Ciesielski and Dr. Masaki Katsumata for their assistance with data acquisition.

The community of the Atmospheric Science Department at Colorado State University deserves my never-ending gratitude. Without the help of such a supportive group, I would never have made it to this point in my meteorology career. Most importantly, thank you to all of the members of the Radar Meteorology Research Group, past and present, whom I had the honor to work with and whom I have not yet mentioned: Julie Barnum, Kyle Chudler, Adam Clayton, Dr. Brody Fuchs, and Marqi Rocque.

This work was supported by NSF grant AGS-1649784, entitled "Analysis of

Convection Observed in Dynamics of the Madden-Julian Oscillation (MJO) (DYNAMO)".

TABLE OF CONTENTS

LIST OF TABLES

LIST OF FIGURES

CHAPTER 1: INTRODUCTION

The Madden-Julian Oscillation (MJO; Madden and Julian 1971, 1972) is a tropical disturbance that propagates across the central Indian Ocean (CIO) and western Pacific Ocean with an intraseasonal cycle of 30-60 days. The MJO is characterized by deep convection initiating over the warm waters of the central Indian Ocean. This convective envelope traverses across the equatorial Maritime Continent to the western Pacific Ocean. Convection eventually dies over the relatively cooler waters of the eastern Pacific Ocean (Zhang 2005) but yet the wave-like MJO envelope circumnavigates the globe. The MJO has far reaching impacts on mid-latitude weather patterns. During late 2011 through early 2012, the comprehensive, international field project Dynamics of the MJO (DYNAMO) was carried out (Yoneyama et al. 2013). DYNAMO's central focus was to characterize atmospheric and upper ocean structure and variability associated with development of the MJO, and how atmospheric and oceanic characteristics evolved through an MJO event. DYNAMO produced an immense volume of radar, sounding, other atmospheric, and oceanic data. A primary goal of our study is to use this vast dataset to compare to findings from data-limited studies on organized convection and relate characteristics of tropical organized convection to the phases of the MJO.

Organized convection, in the form of mesoscale convective systems (MCSs), plays a large role in the vertical transport of horizontal momentum. This transfer of momentum modifies the environmental vertical wind shear (LeMone et al. 1984). LeMone et al. (1984) found this transport of momentum to be a function of MCS organization. They indicated that systems with shear-perpendicular orientation transport momentum up-gradient,

increasing environmental wind shear. Systems with shear-parallel orientation transport momentum down-gradient, decreasing environmental shear. Several studies discuss the organization of tropical convection based on measurements from field campaigns. Such studies include the GARP Atlantic Tropical Experiment (GATE) in the tropical east Atlantic region (LeMone et al. 1984); Tropical Ocean Global Atmosphere Program's Coupled Ocean Atmosphere Response Experiment (TOGA COARE) in the tropical west Pacific warm pool (Jorgensen et al. 1997; LeMone et al. 1998; Kingsmill and Houze 1999); the Equatorial Mesoscale Experiment (EMEX) between Australia and Indonesia (Alexander and Young 1992); and the South China Sea Monsoon Experiment (SCMEX) in the South China Sea (Johnson et al. 2005).

Alexander and Young (1992) found convective lines in EMEX typically aligned perpendicular to the environmental low-level (LL) shear vector. If the LL shear was less than 5 ms^{-1}, convective lines were aligned parallel to mid-level (ML) shear. The dataset of Alexander and Young (1992) was limited to airborne radar data from ten flights. LeMone et al. (1998) found that convective lines in TOGA COARE were less common than in GATE and were faster moving, shear-perpendicular squall lines. They were able to categorize squall line orientation based on the direction of the LL and ML environmental shear, and found that convective lines typically align perpendicular to strong LL shear (1000-800 hPa). When strong LL shear was not present, convective lines aligned parallel to strong ML shear (800-400 hPa). When both strong LL and ML shear are present, the LL shear was shown to determine the orientation of the primary convective bands, while secondary bands aligned parallel to the ML shear. The dataset of LeMone et al. (1998) was limited to 22 events during TOGA COARE. Johnson et al. (2005) built on the work of LeMone et al.

(1998) with similar findings from SCMEX, and their dataset was limited to ten days of ground-based radar. Guy and Jorgensen (2014) also investigated convective organization. Their study took place during DYNAMO, but their data was limited to nine radar convective elements documented by airborne radar. They found that DYNAMO linear features were primarily parallel to weak LL shear. Guy and Jorgensen (2014) suggested that DYNAMO MCSs exhibited a different dynamical structure compared to TOGA COARE, with the DYNAMO systems lacking a descending rear inflow jet in MCSs containing shear perpendicular, linear convection. This type of organization and flow structure is also common in the middle latitudes (Houze 2014).

The aforementioned works relate the environmental shear to the orientation of linear MCSs (Alexander and Young 1992; LeMone et al. 1998; Johnson et al. 2005; Guy and Jorgensen 2014). It has been theorized for some time that the balance between horizontal vorticity due to environmental shear and horizontal vorticity generated by the cold pool ahead of a linear MCS is crucial to the longevity of the MCS (RKW theory; Rotunno et al. 1988; Weisman and Rotunno 2004). The authors advanced that this theory was valid for midlatitude and tropical squall lines, and these systems propagate in the direction of the environmental shear vector (downshear propagation).

Studies by Alexander and Young (1992) and Keenan and Carbone (1992) support the applicability of RKW theory in tropical systems. However, the thermodynamic characteristics of midlatitude MCSs differ from those in the tropics. Tropical systems exhibit very little convective inhibition. They do exhibit considerable convective available potential energy, but that energy is distributed through a much deeper layer than in the case of midlatitude convection. They often form in more weakly sheared environments

compared to the middle latitudes. Also, tropical cold pools are generally weaker than those in midlatitudes (Lane and Moncrieff 2015). Lane and Moncrieff (2015) and Moncrieff and Lane (2015) argue that RKW theory plays a smaller role than originally theorized in tropical systems characterized by weaker cold pools and lower convective inhibition. Lane and Moncrieff (2015) show that MCSs can propagate against the environmental shear vector (upshear propagation), and these systems are maintained by ducted gravity waves. Moncrieff and Lane (2015) looked at downshear propagating systems in the tropics and found that cold pool strength did not control the propagation of MCS leading lines. Grant et al. (2018) also found that propagation of MCSs with tropical characteristics is not affected by cold pool strength. They indicate that environments with low convective inhibition are more susceptible to the destabilizing effects of gravity waves, and this process plays a larger role in MCS propagation than RKW theory.

Moncreiff (1992) put forth an archetype of flow features in linear convection. These features consist of a jump updraft, overturning downdraft, and overturning updraft. Updrafts and downdrafts are responsible for redistributing horizontal momentum via vertical fluxes. Kingsmill and Houze (1999) expanded on the work of Moncrieff (1992) with a more complicated model of MCS flow, yet preserving the flow features described my Moncrieff. Their study utilized airborne dual Doppler radar data from 25 cloud systems during TOGA COARE. They demonstrated that the jump updraft model put forward by Moncrieff (1992) over-simplified the flow patterns within tropical MCSs. Kingsmill and Houze (1999) included the interaction between processes present in the trailing stratiform region of MCSs with those of the convective leading line in their model. This model includes the interaction of sloped, descending stratiform inflows with convective-scale

downdrafts. These findings have important bearings on momentum transport by tropical convection.

Past studies on convective organization in the tropics, including those associated with the MJO, relied on limited datasets using satellite observations or airborne radar. Satellite observations such as those from the Tropical Rainfall Measuring Mission (TRMM) offer limited data only available during certain times of day (Simpson et al. 1988). Airborne radars were able to follow individual events for longer periods of time, but the number of events was limited. The land-based dataset acquired during DYNAMO allowed scientists to observe individual convective features associated with the MJO environment continuously for several months. Zuluaga and Houze (2013) used DYNAMO data to classify the depth and breadth of convection in the central Indian Ocean region. Johnson and Ciesielski (2013) used DYNAMO sounding data to examine the kinematic and thermodynamic characteristics of the MJO. Xu and Rutledge (2015) found that DYNAMO MCSs most frequently took the form of broad stratiform regions with embedded convection. Xu and Rutledge (2014) examined convection characteristics and the precipitation distribution across the MJO. Xu et al. (2014) described the spatial variability of convection in the CIO during DYNAMO. They found that when the MJO was active over the equator, convection became suppressed south of the equator. Kerns and Chen (2014) used reanalysis data to explain spatial variability during DYNAMO, indicating that dry air intrusion was able to redistribute convection from the intertropical convergence zone (ITCZ) to the equator. Barnes and Houze (2014) used polarimetric radar data from DYNAMO to show the distribution of hydrometeor types present in different flow features of MCSs proposed by Moncrieff (1992) and Kingsmill and Houze (1999).

Xu and Rutledge (2015) examined linear MCSs to some degree during DYNAMO, however they did not do an in-depth study on convective organization in relation to environmental wind shear. They also did not examine the flow features of linear MCSs. Guy and Joregensen (2014) addressed both of these questions, but not in detail, and with a sample size of only nine events. In this study, we will also use the vast dataset acquired during DYNAMO address both questions. First, we will address the relationship between the orientation of linear MCSs and the environmental shear during the phases of the MJO. We will also use surface meteorological data to diagnose cold pool strength and assess the validity of RKW theory to convective line propagation. Finally, we will perform an in-depth examination of the flow structures present in these linear systems and compare our findings to those of Moncrieff (1992) and Kingsmill and Houze (1999). In answering these questions, we hope to improve the overall understanding of the vertical transport of horizontal momentum during an MJO cycle. Our findings will also be most useful in validating numerical models that resolve tropical convection.

CHAPTER 2: DATA AND METHODOLOGY

This study utilized radar, sounding, and surface meteorological data from the Dynamics of the Madden-Julian Oscillation (DYNAMO) field campaign. The intensive observation period took place from October through December of 2011 in the central Indian Ocean. Measurements were taken in the vicinity of 8˚S-0˚ latitude and 73˚E-80.5˚E longitude. The DYNAMO array of measurement sites is depicted in Figure 2.1.

2.1. RADAR DATA

2.1.1 RADAR INSTRUMENTS

Radar data from three sites was used in this study. These instruments included two ship borne radars, one on the R/V *Roger Revelle* and another on the R/V *Mirai*. The ship borne radars both operated at C-band (5 cm wavelength). The third radar was an S-band (10 cm wavelength; NCAR S-PolKa), land-based radar on Gan Island.

The R/V *Revelle* was located on the equator at 80.5°E longitude (Xu et al. 2015). It made four deployments to this position between September 2011 and January 2012. The NASA TOGA C-band radar was onboard the R/V *Roger Revelle* (*Revelle* radar) for all four cruises, and operated around the clock while the ship was at its assigned location at a point in the eastern portion of the DYNAMO array. Colorado State University and NASA personnel operated the radar. The *Revelle* radar completed one volume scan every 10 minutes. Each volume included twenty-two 360° plan position indicator (PPI) scans at a range of 150 km and five range height indicator (RHI) scans. Elevation angles for the PPI scans ranged from 0.8° to 21.5° above horizontal. The azimuth angles for the RHI scans were chosen by the radar scientist, and varied by volume. Elevation angles for the RHI

scans were from 0.8° to 40°. The *Revelle* radar data were quality controlled by the Radar Meteorology Group at Colorado State University and NASA (Xu and Rutledge 2014).

The R/V *Mirai* was located at 8°S latitude, 80.5°E longitude (Xu et al. 2015). The ship made two cruises to this position, which was located at the southeastern node of the DYNAMO sounding array. The vessel was also equipped with a C-band Doppler radar (*Mirai* radar) that operated around the clock while the ship was at its assigned location. The *Mirai* radar was operated by the Japan Agency for Marine-Earth Science and Technology (JAMSTEC). Like the *Revelle* radar, it also completed a full volume scan every 10 minutes. The scans included twenty-one 360° PPI scans at 0.5° to 40.0° in elevation with a range of 160 km. RHI scans were collected at the discretion of the radar operator and not taken on regular intervals. Data from the *Mirai* radar were quality controlled by JAMSTEC. Their methods are detailed in Katsumata et al. (2008).

Gan Island, located at 0.6°S latitude, 73.1°E longitude, was the site of three land-based radars during the DYNAMO field campaign (Xu et al. 2015). This study utilized data from the NCAR S-PolKa S-band polarimetric radar (hereafter referred to as S-Pol). Although S-Pol operated at both S- and Ka-bands, only S-band data were used in this study. This radar also operated around the clock during DYNAMO. Unlike the C-band radars, there were no interruptions for port calls. S-Pol made one full volume scan every 15 minutes, collecting PPIs in 360° at eight elevation angles (0.5° - 11°) at a range of 150 km. S-Pol collected RHIs regularly in 54 azimuths between 4° and 82° and between 114° and 140° in increments of 2°. RHI elevation angles ranged from 0° to 45°. Note that S-Pol only collected RHIs looking northeast and southeast from the radar, with no coverage to the

west or south due to beam blockage. NCAR performed the quality control of S-Pol data. Their procedures are detailed in Feng et al. (2014).

2.1.2 DESCRIPTION OF RADAR PRODUCTS

In addition to more convectional weather radar variables of reflectivity (Z) and Doppler radial velocity (V), this study also utilized spectrum width and polarimetric variables including differential reflectivity, specific differential phase, and correlation coefficient. Spectrum width (SW), available for all radars, is the variability of radial velocity in each radar gate. An area of large SW indicates non-uniform motion or turbulent flow. It is helpful in identifying boundaries between flow in different directions. A column of enhanced SW can indicate vertical motion.

The polarimetric variables were only available for S-Pol. Dual polarization radars such as S-Pol send out signals in both the horizontal and vertical planes. Differential reflectivity (Z_{DR}) is the difference between the reflectivity factors in these two planes. Positive Z_{DR} occurs when targets return larger reflectivity in the horizontal plane than the vertical (Herzegh and Jameson 1992). For example, oblate raindrops are associated with positive Z_{DR}. Spherical targets return a Z_{DR} of zero dB. Correlation coefficient (ρ_{hv}) is the correlation between horizontal and vertical reflectivity returns. It decreases in the presence of a non-uniform distribution of particle size, shape, and orientation (Balakrishnan and Zrnic 1990). This value is near unity (0.98-0.99) for uniform drop size distributions. Specific differential phase (K_{DP}) is derived from the phase lag between horizontally and vertically polarized waves (differential phase, φ_{dp}) passing through oblate targets like raindrops (Jameson 1985). The quantity φ_{dp} is cumulative with range but radar processing can measure the phase lag at each radar gate. K_{DP} is defined as the change in

φ_{dp} with range, divided by two since phase shift occurs for two-way propagation (Bringi and Chandrasekar 2001). The magnitude of K_{DP} is dependent on the number of scatterers present (liquid water content) and mass-weighted oblateness. Since large raindrops are more oblate compared to small drops, K_{DP} is significant in areas of intense rain. A more in-depth discussion of these polarimetric radar variables can be found in numerous textbooks including Bringi and Chandrasekar (2001).

Although data from all three radars were quality-controlled prior to this study, some additional unfolding (dealiasing) of velocity data was necessary for the *Revelle* and *Mirai* radars. This procedure was performed using the Python ARM-Radar Toolkit (Pyart; Helmus and Collis 2016). Pyart provides automated algorithms to dealias Doppler velocity data. Any data that were subject to Pyart's automated algorithms were also visually inspected to assure that Pyart was able to correctly dealias the data.

2.2 SOUNDING AND SURFACE METEOROLOGY DATA

Atmospheric soundings were launched from all three radar sites eight times per day during the DYNAMO intensive operations period. The data were quality controlled as detailed in Ciesielski et al. (2014). Radiosonde launches took place at 0200 UTC and every 3 hours thereafter. Profiles of pressure and wind were used to calculate environmental shear

Thirty-second surface meteorological data was acquired from the DYNAMO Field Catalog for the *Revelle* location. Thee variables were collected with NCAR's Integrated Sounding System (UCAR/NCAR 2016). One minute surface meteorological data was also maintained at the S-Pol radar site (http://dynamo.ml-ext.ucar.edu/dynamo_legacy/). Surface meteorological data for the *Mirai* radar site was acquired via personal contact with

Masaki Katsumata of JAMSTEC (March 6, 2019). These meteorological measurements included surface temperature, pressure, relative humidity, wind speed, and wind direction. These variables were used to identify cold pool passages over each radar site.

2.3 PHASES OF THE MJO

Much of this study involves examining the relationship between the organization and prevalence of MCSs and MJO phase. To do this, we needed a way to quantify the MJO. The Wheeler-Hendon Real-time Multivariate MJO Index (Wheeler and Henden 2004) assigns a phase of 1 through 8 to each day in the tropics. It is based on outgoing longwave radiation (OLR) and the wind fields at 850 and 200 hPa. Active (inactive) phases occur during periods of low (high) OLR, and, therefore, are periods of higher (lower) cloud fraction, higher (lower) precipitation, and more (less) convective activity (Xu and Rutledge 2014). The active MJO phases for the central Indian Ocean are phases 2 and 3. Inactive phases are all others, however phases 1 and 4 are considered pre- and post-onset, respectively, while phases 5-8 are suppressed (Xu and Rutledge 2014). Figure 2.2 depicts MJO propagation over the central Indian Ocean.

2.4 PRECIPITATION FEATURE IDENTIFICATION

A large part of this study required identifying precipitation features (PFs) that met the criteria for a linear MCS. We defined such a system by using the criteria put forth by Rickenbach and Rutledge (1998) for their classification of "MCS linear" events. These features are at least 100 km in length and have a major to minor axis ratio of at least 5:1. They typically consist of a convective band along with stratiform precipitation that leads, trails, or at times, is parallel to the convection. These criteria are consistent with previous studies by LeMone et al. (1998), Kingsmill and Houze (1999), Guy and Jorgensen (2014),

and Xu and Rutledge (2015), as well as the definition of "MCS" proposed by Houze (2004). To be considered an individual PF, an event had to exist in the radar PPI reflectivity field for at least 30 minutes.

We analyzed the PPI reflectivity fields from each of the three radars using an algorithm developed by Xu and Rutledge (2014) to obtain a list of PFs that met our criteria. This algorithm is able to pick out PFs from the reflectivity field by looking for contiguous areas of pixels exceeding 17 dBZ at 2 km in elevation (Xu and Rutledge 2014). This algorithm is capable of classifying major convective features within a PF using 30 dBZ as the threshold for convection. For each PF identified, a list of descriptive fields including area, stratiform area, major axis length, minor axis length, convective major axis length, convective minor axis length, and orientation angle are retrieved. Figure 2.3 shows a PPI of a linear PF from the S-Pol radar and serves to illustrate a typical PF and how descriptive fields from the output of the PF identification algorithm are dimensioned. In addition to these descriptive fields, the output includes the date and time of the scan, as well as the x- and y-coordinates of the centroid of each PF. The coordinates are in units of kilometers either north-south or east-west of the particular radar. Aspect ratio is calculated as:

$$Aspect\ Ratio = \frac{Convective\ minor\ axis\ length}{Convective\ major\ axis\ length}.$$

We can also query the list by length (major axis length) to be greater than 100 km and aspect ratio to be less than or equal to 0.2.

The next step in identifying linear PFs of interest was to visually inspect the PPI reflectivity field for each individual feature in the query output, grouping consecutive scans into PFs that fit the criteria for length, aspect ratio, and duration. The final step was to take another close look at each PF that fit our criteria and decide if there was any other reason it

should be discarded. One common reason for discarding a PF was that it was located at the fringe of the radar's range. The result was a PF that appeared linear to a computer algorithm, but only because a sliver of the entire feature was visible by the radar. Such events were discarded because, without seeing the entire feature, it was impossible to know whether that PF was truly linear and, if so, what its orientation was. The final result was a list of linear PFs from each radar site with known aspect ratio, length, and orientation angle. These metrics are averaged over the lifetime of each PF.

2.6 COLD POOLS AND LINE SPEEDS

Identifying cold pools was done using PPI radar scans of reflectivity and surface meteorology data at each observing site. Only PFs that passed over one of the three radar sites were used in this section of the study. Line speeds were calculated by measuring the distance the leading edge of a convective line travelled over consecutive scans. The direction was defined in accordance with Alexander and Young (1992). They chose the line speed to be in a direction perpendicular to the line orientation. Cold pool strength was measured from the surface meteorological data as the drop in temperature that occurred just prior to the convective line passing over the measuring site. Increase in wind speed, change in wind direction, and increase in relative humidity were also taken into account when identifying a temperature drop associated with a cold pool. Figure 2.4 shows an example meteogram and associated PPI reflectivity scan of a *Revelle* cold pool event.

The theoretical cold pool speed in ms^{-1} was then taken as:

$$c = \sqrt{\frac{\theta'_{\rho\min}}{\overline{\theta_v}} gH} \qquad (2.1)$$

where $\theta'_{\rho min}$ is the perturbation potential temperature decrease in degrees Kelvin, $\overline{\theta_v}$ is the mean ambient virtual potential temperature in degrees Kelvin, g is the acceleration due to gravity in ms^{-2}, and H is the depth of the cold pool in meters. (Markowski and Richardson 2010). Measuring H proved to not be possible using the data set available in DYNAMO. The tropical ocean environment is very clear, providing little, if any, scatters outside of precipitation areas. Without scatterers, the cold pool boundary was rendered undetectable by weather radar. We chose H to be a constant 500 m deep based on the modeling results of Grant et al. (2018)'s study of cold pools in tropical convective systems. Lane and Moncrieff (2015) and Moncrieff and Lane (2015) assume H to be 1000 m. They give no justification for their assumption. Since Grant et al. (2018) used an H that was the mean depth of a the cold pool from simulated tropical MCSs, we conform to their study.

2.7 RHI INVESTIGATIONS

Assessment of air flow patterns within linear PFs was done using RHI scans from each radar. Not all PFs used in previous sections were used in this part of the study. Limiting factors included:

1. The distance between the PF in question and the radar,
2. The RHI scanning strategy, and
3. The orientation of the PF.

The distance between the PF and the radar limited inclusion if the PF was more than 100 km from the radar. At this distance, radar sample volumes are large, degrading the resolution of all radar fields. The RHI scanning strategy became a limiting factor when a well-formed PF was within 100 km but not visible by the azimuths scanned during radar operation at that time. In the case of S-Pol, RHI scans were only taken in the northeast

quadrant and parts of the southeast quadrant. So, if a PF approached from the west and dissipated before moving to the east of the radar, no RHI scans were available. In the case of the *Revelle* and *Mirai*, RHI scans were taken at the discretion of the radar scientist. If the radar scientist chose not to scan in the direction of a PF, obviously no RHI was available. Finally, PF orientation was a limiting factor. Only PFs oriented approximately perpendicular to the radar beam were used. If a PF was oriented parallel to the radar beam, the Doppler velocity field would not be useful because motion of the PF would be perpendicular to the beam.

In addition to radar fields detailed in Chapter 2.1, two additional fields were calculated from the Doppler velocity field: storm-relative velocity (VSR) and horizontal divergence. Storm-relative velocity was calculated by subtracting the motion vector of a PF from its Doppler velocity field. Storm motion was determined by examining the PPI reflectivity field, noting how far the leading edge of a line travelled over a known time period. Before calculating horizontal divergence and vertical velocity, the storm-relative velocity data was interpolated onto a Cartesian grid from radar coordinates. Horizontal divergence was then calculated along the radar beam as

$$DIV_H = \frac{dv_r}{dr} \tag{2.2}$$

where DIV_H is the horizontal divergence, v_r is the storm-relative radial velocity and dr is the gate spacing along the radar beam, typically 150 m.. DIV_H was then smoothed using a Gaussian filter with a standard deviation of 6.0.

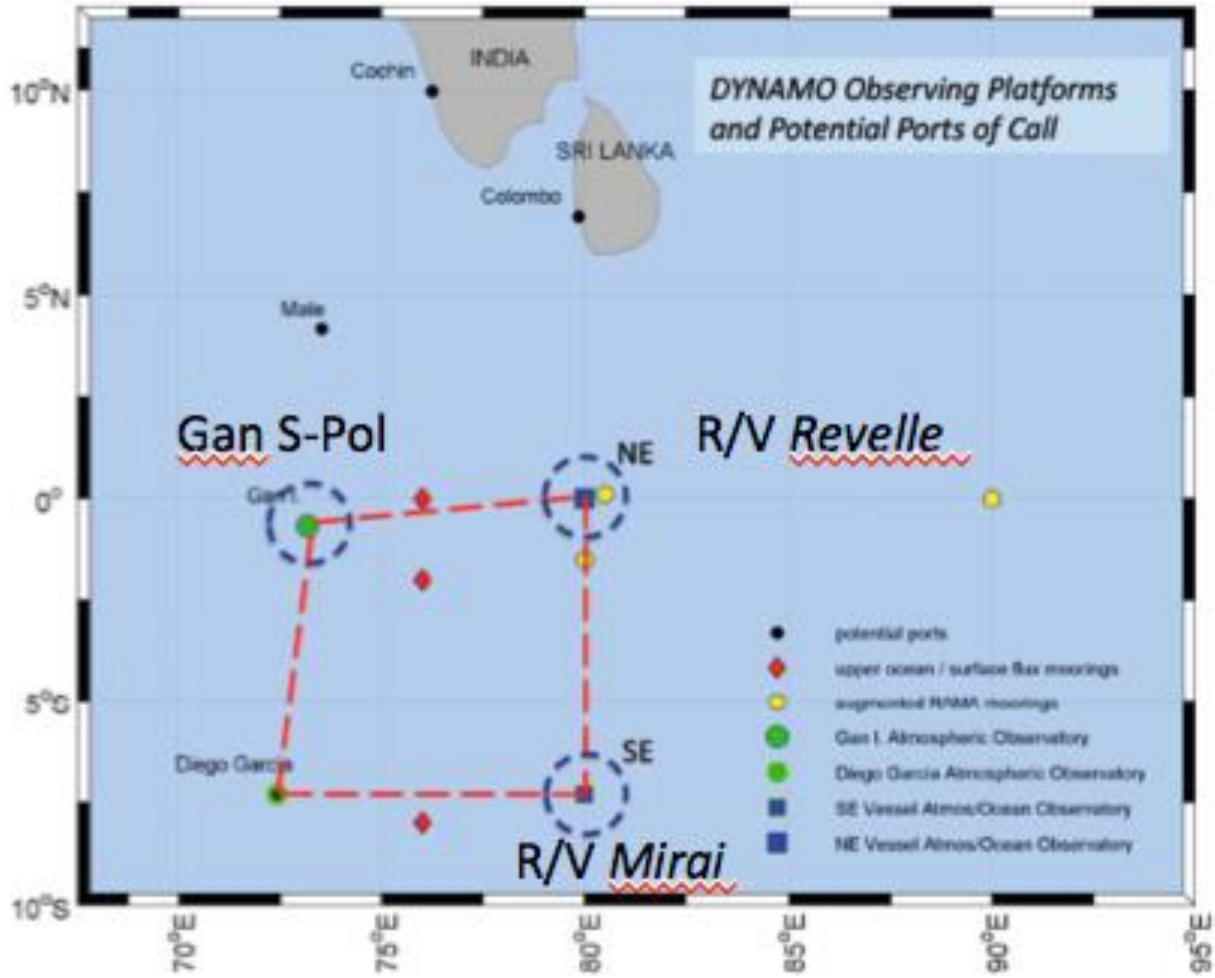

Figure 2.1. The DYNAMO study area showing the locations of the three measuring sites used in this study.

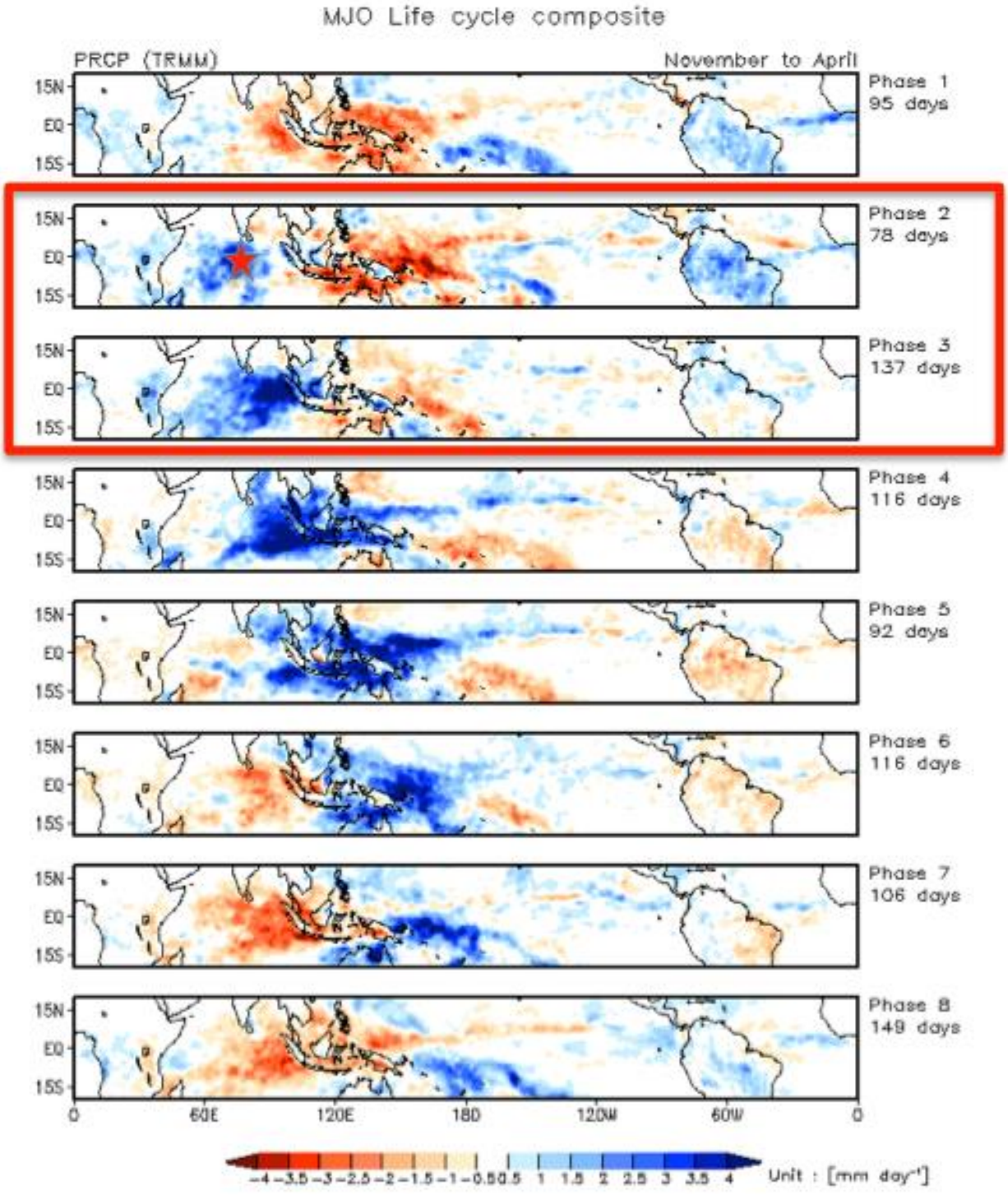

Figure 2.2. An illustration of an MJO lifecycle composit. The DYNAMO study area is starred on Phase 2. Color fill is TRMM precipitation anomaly. The active phases of the MJO for the DYNAMO study area are in the red box, Phases 2 and 3.

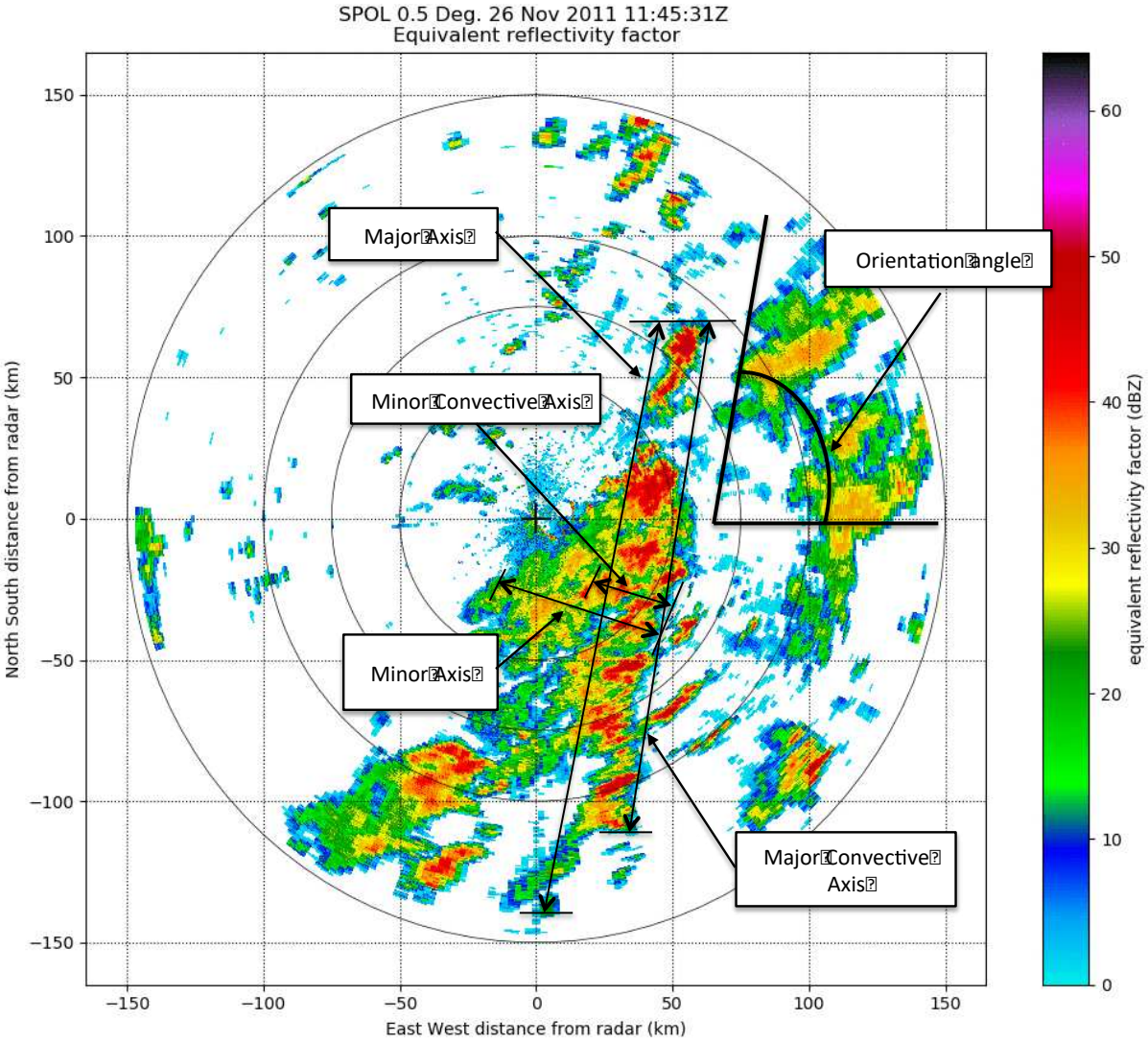

Figure 2.3. An example of a linear precipitation feature, with typical dimensions of descriptive fields labeled. This line is moving away from the S-Pol radar, from west to east.

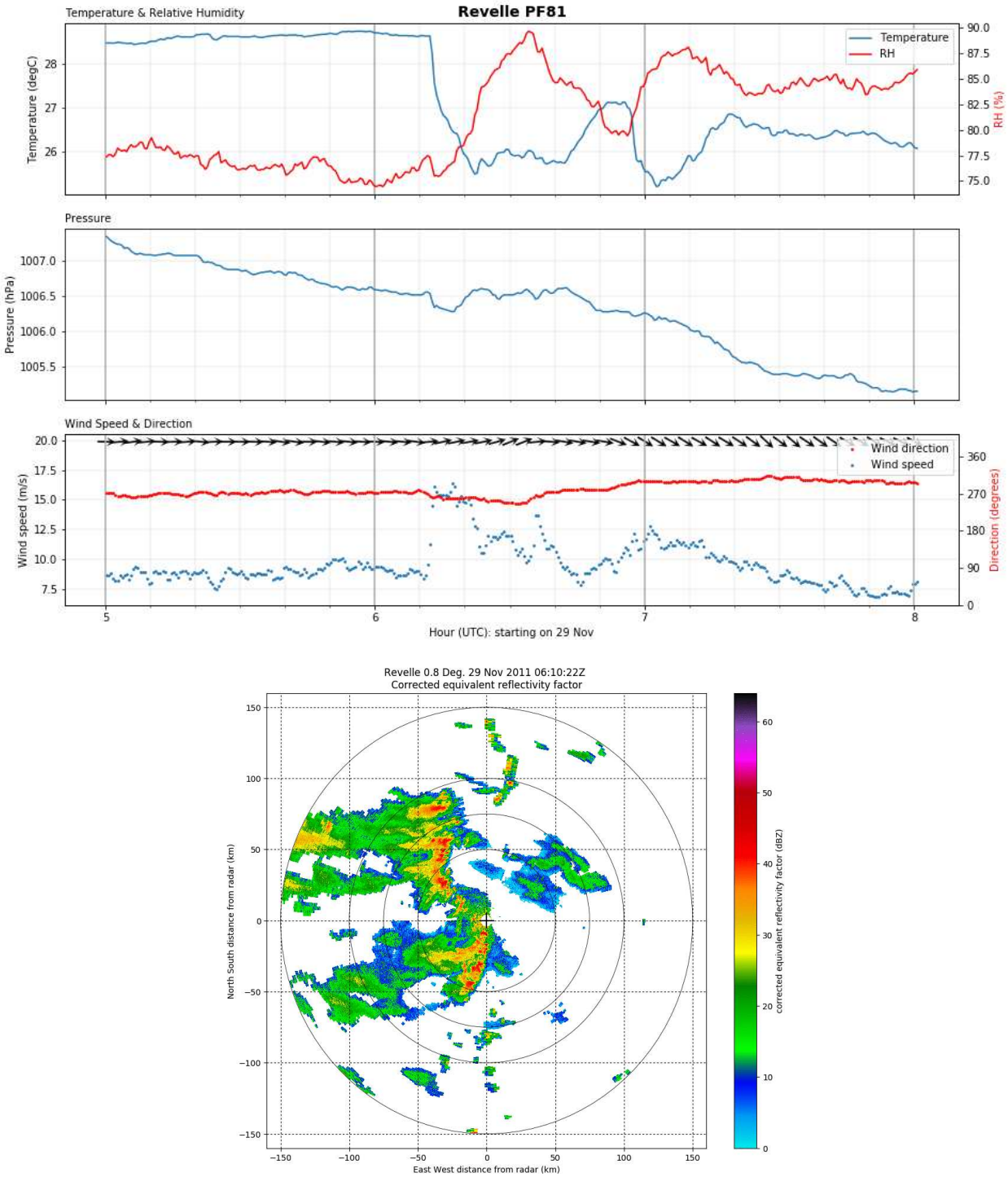

Figure 2.4. An example of a cold pool passage over the *Revelle* radar. Note the sudden decrease in temperature and associated increase in relative humidity. Although the wind direction did not change, the wind speed increased. This convective line is moving from west to east.

CHAPTER 3: ORGANIZATION OF LINEAR PRECIPITATION FEATURES

3.1 CLASSIFICATION OF LINEAR PRECIPITATION FEATURES OVER THE MJO

3.1.1 RELATIONSHIP OF LINEAR PRECIPITATION FEATURES TO ENVIRONMENTAL SHEAR

To classify linear PFs as shear parallel or shear perpendicular to the LL or ML shear, we use the framework put forth by LeMone et al. (1998). Johnson et al. (2005) modified this framework, and Figure 3.1 depicts a schematic of their specific types of convective organization. They found that linear systems typically aligned themselves to the environmental shear in the following manner:

1. In the absence of strong LL and ML shear, convection was aligned with outflow boundaries, convective lines were not continuous, and convection was smaller than an MCS (length was less than 100 km).
2. In the presence of strong LL shear (> 4 ms^{-1}) and weak ML shear (< 5 ms^{-1}), linear systems were aligned perpendicular to the LL shear. When there was dry air aloft and deep convection was not possible, convective lines aligned parallel to the LL shear (type 2r).
3. In the presences of strong ML shear (> 5 ms^{-1}) and weak LL shear (< 4 ms^{-1}), linear systems align parallel to the ML shear.
4. In the presence of both strong LL shear and strong ML shear, linear systems were aligned perpendicular to the LL shear in most cases. They were also aligned parallel to the ML shear (4a), or produced trailing secondary bands parallel to the ML shear (4b). In mode 4c, strong LL and ML shear conditions exist and are in the same

direction. In this case, linear features align themselves parallel to the shear at both levels.

Because type 1 features are not linear and not large enough to be considered MCSs, this study did not consider this mode of organization. Furthermore, small features such as these would be poorly identified by the PF detection algorithm (Xu and Rutledge 2014). Type 1 features appear on the radar as scattered, discontinuous convection producing little precipitation. Some PFs did not fit into any of the modes, and were deemed 'unclassifiable' (U).

For every PF, the LL and ML environmental shear vectors were determined from the sounding data. The shear vector was compared to the orientation angle of the PF. To be considered shear perpendicular (parallel) at either level, the PF needed to be within 30° of perpendicular (parallel) to the shear vector at that level. We chose ±30° as our threshold to be consistent with LeMone et al. (1998). Johnson et al. (2005) required the orientation angle be ±20° for perpendicular and parallel configurations. Alexander and Young (1992) and Guy and Jorgensen (2014) did not specify any criterion for a perpendicular or parallel designation. Each PF was then assigned a mode based on Figure 3.1 of type 2, 2r, 3, 4a, 4b, 4c, or U. Figures 3.2 through 3.5 show examples of types 2, 3, 4a, and 4b. In each figure, a PPI scan of the PF is shown, along with the storm motion and the direction of the LL and ML shear. LL and ML shear is designated as strong or weak. The designation is noted on the figures.

Figure 3.6 is a frequency distribution of the difference between PF orientation angle and direction of the LL and ML shear vector at each site. If this difference is 90° (±30°), the linear PF is perpendicular to the shear at that level. If the difference is 0° or 180° (±30°), it

is parallel. The angles are shown as the smallest angles between the two vectors. The angles are also broken down by shear magnitude (in m s^{-1}). Higher magnitudes indicate stronger shear. The equatorial sites show a shear perpendicular signal at LL and a shear parallel signal at ML. The *Mirai* site is more convoluted.

For both the equatorial sites and the *Mirai*, PFs fit the modes set forth in Figure 3.1. Figure 3.7 shows the frequency of PF type for both the equatorial sites and the off equator site of the *Mirai*. On the equator, many of the PFs (42%) were observed in an environment of both strong LL and ML shear (type 4a, 4b, or 4c). Of the 153 identified PFs, 45% were 'shear perpendicular' (type 2, 4a, or 4b). Thirty four percent were 'shear parallel' (type 2r, 3, or 4c). Twenty one percent of the PFs were unclassifiable in terms of shear. Off the equator, at the *Mirai*, PFs were more closely orientated parallel to strong ML and LL shear. Forty three percent were 'shear parallel' and 28% were 'shear perpendicular'. Twenty eight percent were unclassifiable.

These results are consistent with both LeMone et al. (1998) and Johnson et al. (2005). LeMone et al. (1998) identified 22 PFs, 19 of which were larger than 'small scale'. This 'small scale' designation renders the identification of "linearity" difficult. LeMone et al. found that 6 PFs were not classifiable (31%), 7 were 'shear perpendicular' (37%; type 2 or 4), and 5 were 'shear parallel' (26%; type 3). Their study took place at latitudes varying from 14°S to the Equator. Johnson et al. (2005) did not count individual PFs. They noted typical line orientation, as well as LL and ML shear orientation, during 6-hour time periods centered on radiosonde launches. They refined the archetypes put forth by LeMone et al. (1998) by adding types 2r and 4c. Although a direct comparison to their study is difficult, they found that LL 'shear-perpendicular' periods occurred 10 times (27%; types 4a, 4b, 2),

'shear parallel' periods occurred 13 times (35%; types 3, 2r, 4c), and 9 periods were unclassifiable (24%). Their study took place at 20.4°N latitude.

Although our results do not match previous studies exactly, the linear systems we observed do fall into the archetypes set forth by previous studies as illustrated in Figure 3.1. PFs observed during DYNAMO were organized similarly to those observed during TOGA COARE. We will show that 45% of DYNAMO PFs were shear-perpendicular and 34% were shear-parallel. For TOGA COARE, LeMone et al. (1998) found that 37% were shear-perpendicular and 26% were shear-parallel. A direct comparison is difficult with Alexander and Young (1992), Johnson et al. (2005), or Guy and Jorgensen (2014) due to the nature of the individual studies. Guy and Jorgensen (2014) state "… DYNAMO MCSs were linearly organized more parallel to the low-level shear… than in TOGA COARE." Our findings do not support their statement. Discrepancies between their study and ours are most likely due to their small sample size.

3.1.2. EFFECTS OF THE MJO

Atmospheric variability associated with the MJO was a central focus of the DYNAMO field campaign. This section examines the relationship between MJO phase and PF organization and relationship to LL and ML shear. To evaluate the relevance of the MJO on the results from the previous section, the characteristics of the PF dataset were further broken down by MJO phase.

Figure 3.8 displays the frequency of linear PF occurrence by phase of the MJO for the equatorial and off-equatorial sites. Phase 2 of the MJO along with the pre-onset phase (1) and post-onset phase (4) were most conducive to the formation of linear PFs on the equator. Collectively, 71% of observed PFs on the equator occurred in half of the MJO

phases. These phases were the active phases (2, 3), pre-onset (1), and post-onset (4) phases. PFs were more frequent during active MJO phases south of the equator as well. Most PFs were observed during the active phases, with no activity at all in phases 4 and 5.

Figure 3.9 is similar to Figure 3.6. It depicts the difference between the LL and ML shear direction and PF orientation at the equatorial sites for all MJO phases, active phases, and inactive phases. During the active phases, the LL shear-perpendicular signal intensified, as did the ML shear-parallel signal. Figure 3.10 is similar to Figure 3.7. It depicts the frequency of PF type for all MJO phases (same as Figure 3.7), active phases, and inactive phase. Figure 3.10 shows a slight increase in PF types that depend on LL shear perpendicular and/or ML shear parallel organization (types 3, 4a, and 4c). The decrease in type 2 PFs can be attributed to an increase in ML shear, making PFs with weak ML shear less prevalent. Unclassified PFs became less frequent during the active MJO phases. During the inactive MJO phases, there was a decrease in the frequency of type 4a PFs. This can be attributed to a decrease in the frequency of both LL shear perpendicular and ML shear parallel organizations. There is, however, an increase in the frequency of types 2 PFs. This can be attributed to a decrease in ML shear during the inactive MJO phases. The decrease in frequency of ML shear parallel PFs explains the decrease in frequency of type 3 and 4c PFs. Unclassified PFs are more prevalent during the inactive phases than the active phases.

In Figure 3.11, at the *Mirai*, an increase in LL shear-perpendicular PFs also occurs during the active MJO phases. A response in the ML shear to the onset of an MJO is not evident. During the inactive MJO phases, there was an increase in LL shear-parallel PFs. ML shear during this time lacks any detectable signal, but becomes weak (< 5 m s^{-1}). Figure 3.12 reflects those trends. During the active phases, there was an increase in PF types that

depend on LL shear-perpendicular organization (2, 4a, 4b) and a dramatic drop in frequency of PFs that depend only on LL shear parallel organization (2r). During the inactive phases, type 2r PFs became more frequent in response to the shift of the LL shear to becoming more parallel and the weakening of the ML shear. PF types tied to strong, perpendicular LL shear and/or ML shear-parallel organization were significantly reduced, if not absent altogether (2, 4a, 4b, 4c). Type 3 PFs probably increased due to the lack of any strong LL shear-perpendicular events. The frequency of unclassified PFs increased dramatically during the inactive phases at the *Mirai*.

There was a strong signal between the active and inactive phases of the MJO at both locations. On the equator, these signals were in the form of increased LL shear-perpendicular and ML parallel organization during active MJO phases. This lead to an increase in frequency of type 3 and 4 PFs compared to the same frequency during all MJO phases. At the *Mirai*, there is also an increased level of organization during the MJO active phases. The frequency of LL shear-perpendicular organization increased. The strength of both the LL and ML shear at the *Mirai* dropped off considerably during the inactive phases. This resulted in PFs that were mostly unclassifiable or exhibited either weak LL or weak ML shear (types 2r and 3). Overall, the *Mirai* exhibited a larger frequency of unclassifiable PFs.

Knowing how phases of the MJO are defined, it was expected that more convective activity would occur during active phases during DYNAMO. Our results supported this conclusion and agreed with previous studies of the DYNAMO field campaign. Zuluaga and Houze (2013) found that MJO active phases were more favorable for convection at S-Pol site. Guy and Jorgensen (2014) also found that MJO active phases included 'more robust

convection' versus inactive phases based on DYNAMO aircraft radar. Xu and Rutledge (2014) noted that the frequency of PFs at the *Revelle* that were able to reach mesoscale size peaked in phase 2, with phase 3 characterized by weaker convective cores. Finally, Xu and Rutledge (2015) also used the *Revelle* radar to show that the maximum precipitation from MCSs occurred during the active phases of the MJO.

The difference between PF organization on the equator versus at the *Mirai* warrants further investigation. Previous works agree that the equatorial sites were more favorable for organized convection during DYNAMO. For example, Johnson and Ciesielski (2013) found that the northern DYNAMO observation array captured the strongest convective signal in the form of larger outgoing long-wave radiation anomalies. Kerns and Chen (2014) suggested that dry air intrusion in the southern intertropical convergence zone (ITCZ) suppressed convection south of the equator during DYNAMO. As a result, convection became favored along the equator. Most notably, Xu et al. (2015) did an in-depth analysis of spatial variability of convection during DYNAMO. They found some significant differences between convection at the equatorial sites and the *Mirai*. For example, satellite data showed that precipitation during MJO phases 1 and 2 favored the equatorial sites. Radar data showed that the equatorial sites experienced deeper, more organized convection compared to shallower, isolated convection at the *Mirai*. They also showed that environmental conditions at the *Mirai* varied less across the MJO than those at the equatorial sites. Finally, they indicated that the *Mirai* experienced active convection when the equatorial sites were under suppressed conditions, but became suppressed when the equatorial sites began to experience active conditions. They cite several processes involving the ITCZ, including the ideas of Kerns and Chen (2014), as an explanation for the

difference between convection on and off of the equator. While our results do not support all of the previous findings, they do indicate that the orientation of linear convection depended more on the LL and ML shear at the equator as opposed to south of the equator, at the *Mirai*.

3.2 THE ROLE OF COLD POOLS ON PRECIPITATION FEATURE LINE SPEED

In this section, we look at the relationship between the cold pool and the propagation of linear PFs. Rotunno et al. (1988) and Weisman and Rotunno (2004) introduced the idea that circulation induced by a cold pool ahead of advancing convection interacts with environmental shear to strengthen or weaken the convection. If the cold pool circulation is in balance with the environmental shear, conditions are favorable for prolonged, intense and upright convection. As the cold pool becomes out of balance with the environmental shear from a vorticity perspective, the system weakens. Rotunno et al. (1988) claim that this process was applicable to both midlatitude and tropical environments. In theory, the speed of the cold pool density current would be equal to the propagation speed of a convective line. Various studies have tested this idea. Alexander and Young (1992) found some correlation with line speed and front to rear flow, which they use as a predictor for density current speed. Keenan and Carbone (1992) also found a positive correlation between line speed and density current speed. Lane and Moncrieff (2015) found that the cold pool defined the propagation speed of linear systems in tropical environments. However, this result was for upshear-propagating systems. For downshear-propagating systems, they found no such relationship (Moncrieff and Lane 2015). Most of the PFs in this study were downshear-propagating systems. Grant et al. (2018) also found

that cold pool strength and, therefore, density current speed did not play a role in the propagation of linear systems.

Figure 3.13 shows the relationship between PF line speed and the theoretical density current speed (c) for all sites during all MJO phases, active MJO phases only, and inactive MJO phases only. We identified 35 PFs that passed over an observing site such that we could determine the cold pool thermal properties. Our results back up the previous works that do not find a significant correlation between cold pool strength and line speed (e.g., Moncrieff and Lane 2015; Grant et al. 2018). Looking at MJO active phases only, the results improve slightly but still do not show a strong relationship. Outside of the MJO active phases, the relationship deteriorates. One result that does jump out from Figure 3.13 is the line speed of shear-parallel systems (blue) versus shear-perpendicular systems (red). Shear-parallel systems tended to be slower moving than shear-perpendicular. This result supports the findings of Barnes and Sieckman (1984) and LeMone et al. (1984), each of whom found that vertical wind shear was perpendicular to fast-moving lines and parallel to slow-moving lines during the GATE field campaign just north of the equator, off the coast of West Africa in the Atlantic Ocean.

Most of the PFs used in this section were from the equatorial sites. Figure 3.14 is the same as Figure 3.13, but for equatorial sites only (that is, Mirai PFs are excluded). During active MJO phases, the relationship between line speed and density current speed showed some improvement, and results were similar to those of Alexander and Young (1992). Overall, the results from this section were successful in providing evidence that line propagation in tropical systems does not depend on the speed of the density current. Grant et al. (2018) proposed that gravity waves play a larger role in line speed than the

density current speed. They showed that MCS speed closely corresponded to gravity wave speed in model simulations. These waves were conducive to low-level ascent, destabilization of the lower atmosphere, and convective development. Since these processes are also present in an advancing gust front, distinguishing the role of cold pools from gravity waves in triggering, or sustaining convection is often difficult.

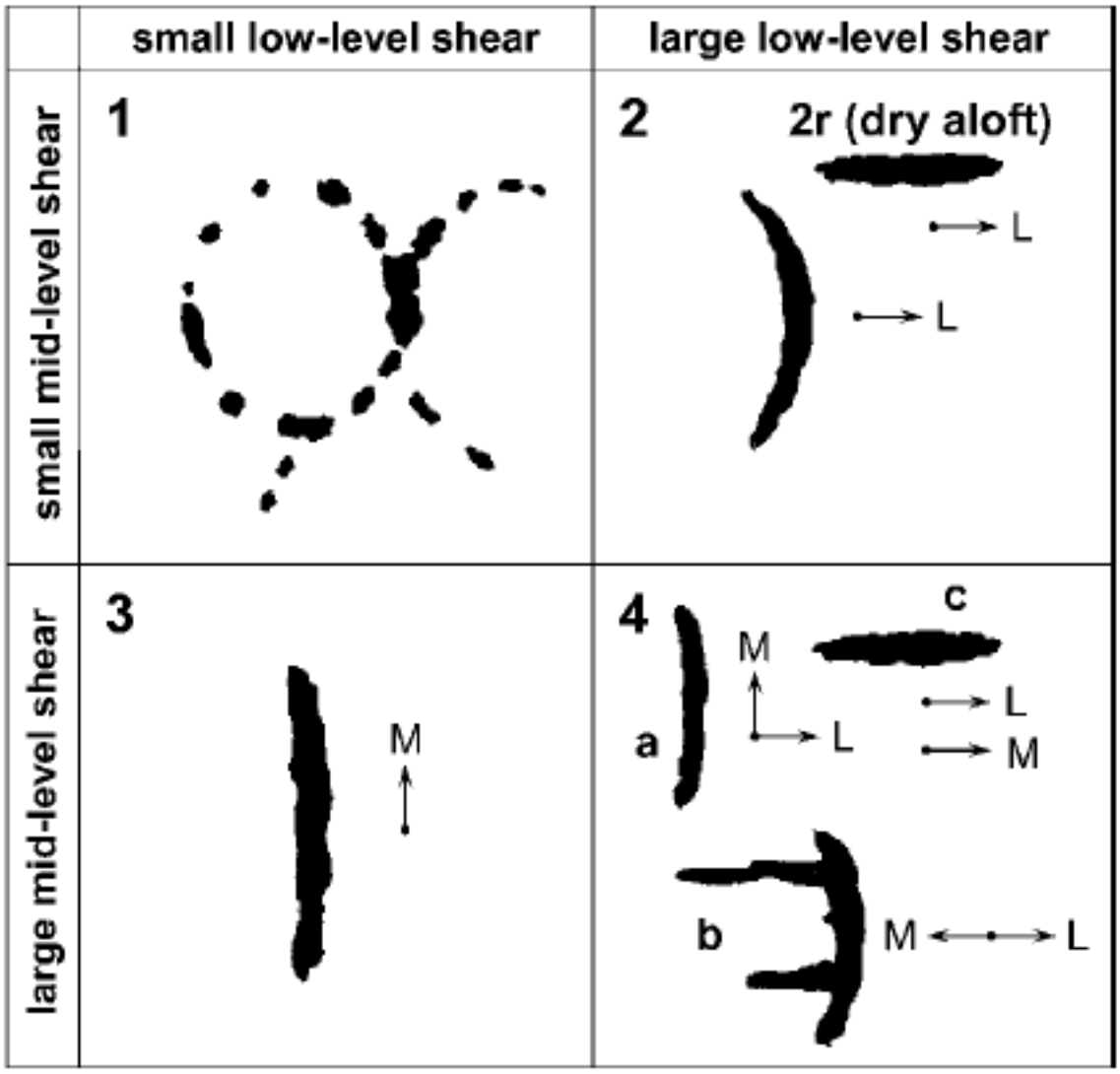

Figure 3.1. Schematic diagram from Johnson et al. (2005), adapted from LeMone et al. (1998), based on results from TOGA COARE and SCSMEX. The lines represent convective bands. The arrows represent the direction of strong mid-level vertical shear (800-400 hPa) and strong low-level vertical shear (1000-800 hPa). The thresholds for strong low- and mid-level shear are 4 ms^{-1} and 5 ms^{-1}, respectively. Convective lines in types 2 through 4 are large enough to be considered an MCS and are longer than about 100 km.

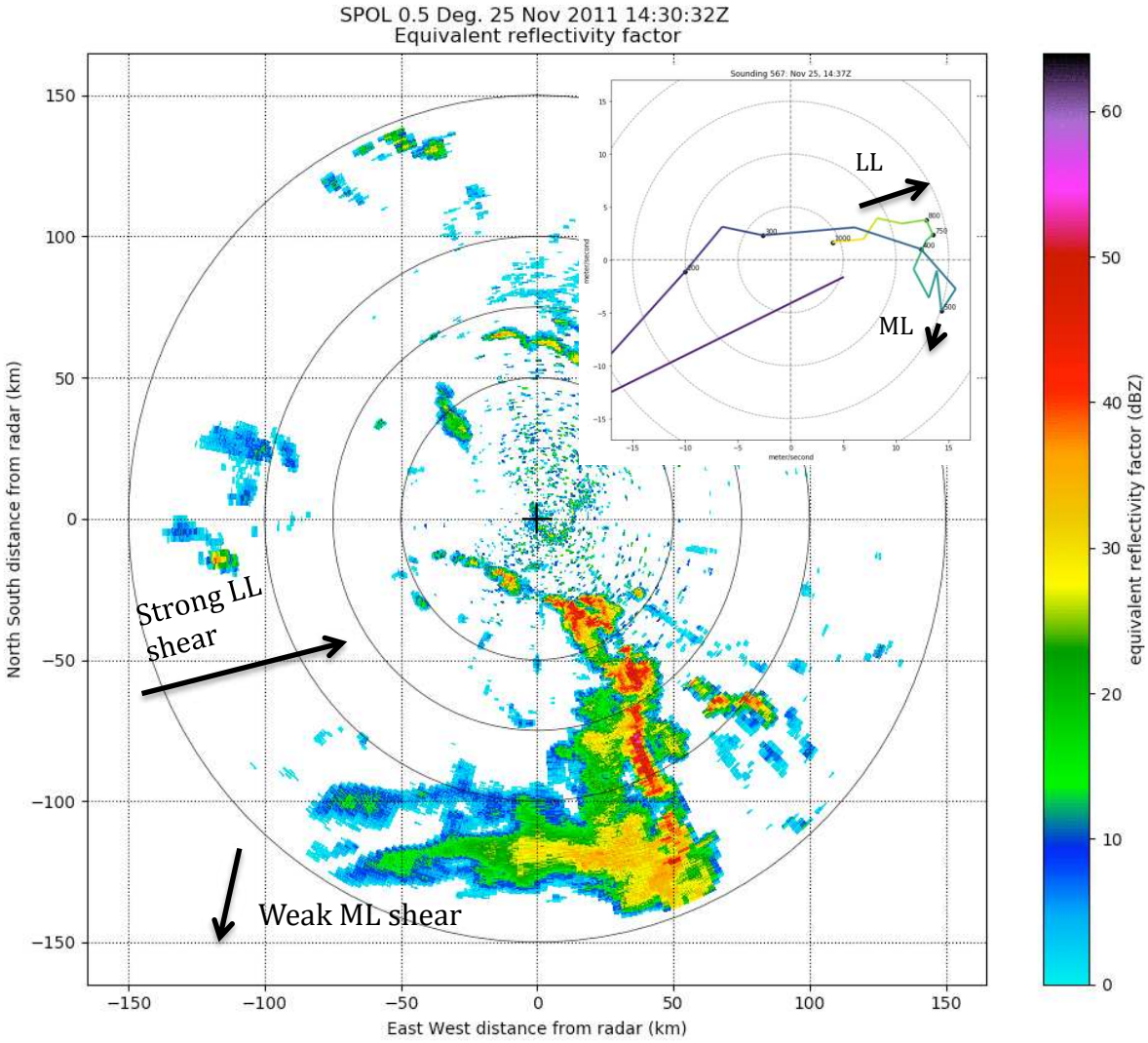

Figure 3.2. An example of a type 2 linear PF. The hodograph used to calculate the shear is inset on the PPI scan. The direction of the ML and LL shear is depicted on the hodograph and on the PPI scan. This PF exhibited strong, perpendicular LL shear and weak ML shear. It is moving from west to east.

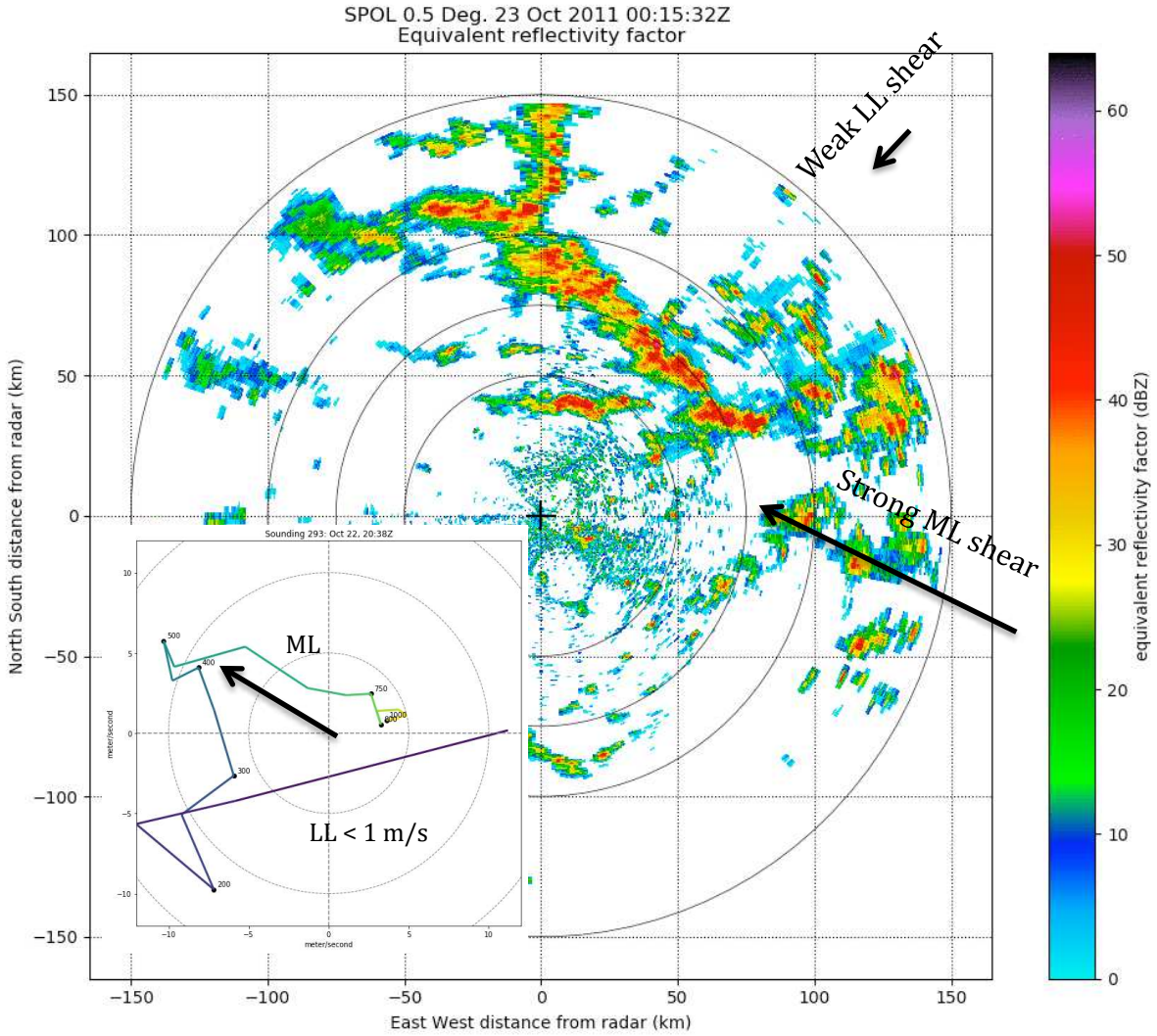

Figure 3.3. An example of a type 3 linear PF. This PF exhibited strong, parallel ML shear and weak LL shear. This PF is moving from northeast to southwest. The LL shear is too small to depict on the hodograph.

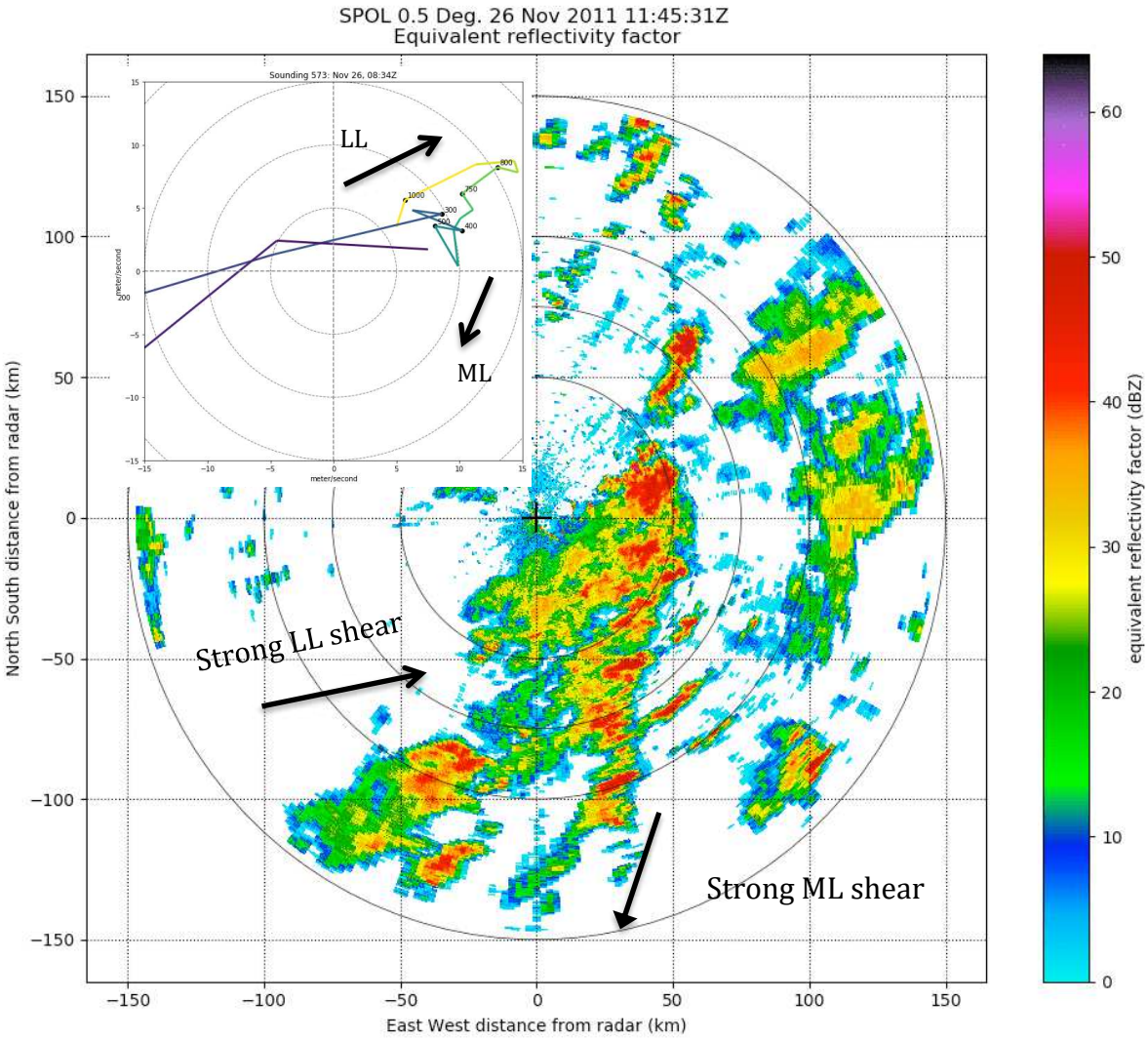

Figure 3.4. An example of a type 4a linear PF. This PF exhibited strong, parallel ML shear and strong, perpendicular LL shear. This PF is moving from west to east.

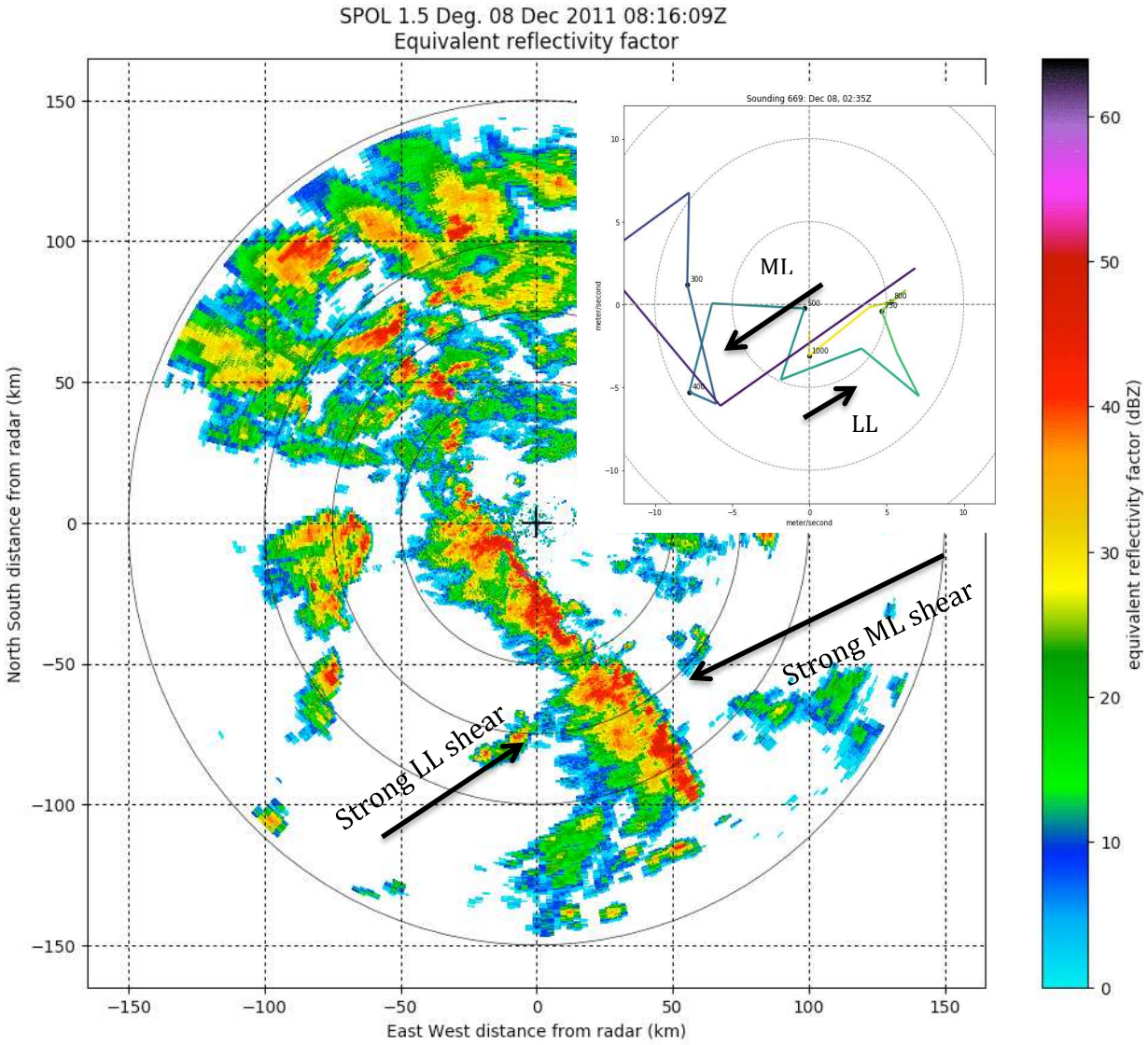

Figure 3.5. An example of a type 4b linear PF. This PF exhibited strong, strong, perpendicular LL shear and strong ML shear. The ML shear is parallel to trailing bands. This PF is moving from southwest to northeast.

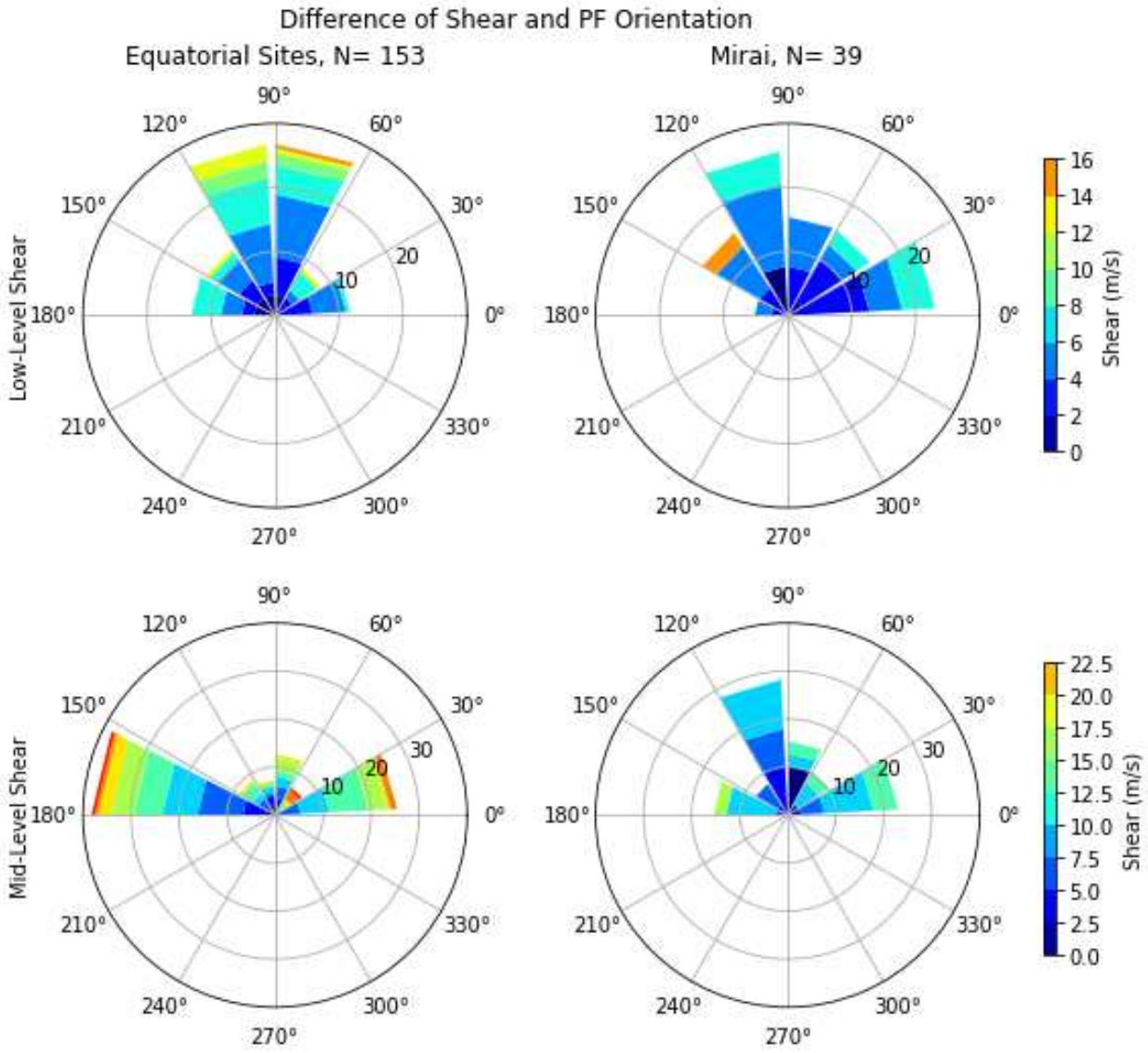

Figure 3.6. Frequency of the difference between PF orientation angle and LL (top row) or ML shear (bottom row) at each site (columns). A difference of 90° (±30°) indicates the shear is nearly perpendicular to the PF orientation. A difference of 0° or 180° (±30°) indicates the shear is nearly parallel to the PF orientation. Angles are computed as the smallest angle between the two vectors. Shear is also broken down by strength. Four and 5 m/s are the threshold for strong LL and ML shear, respectively.

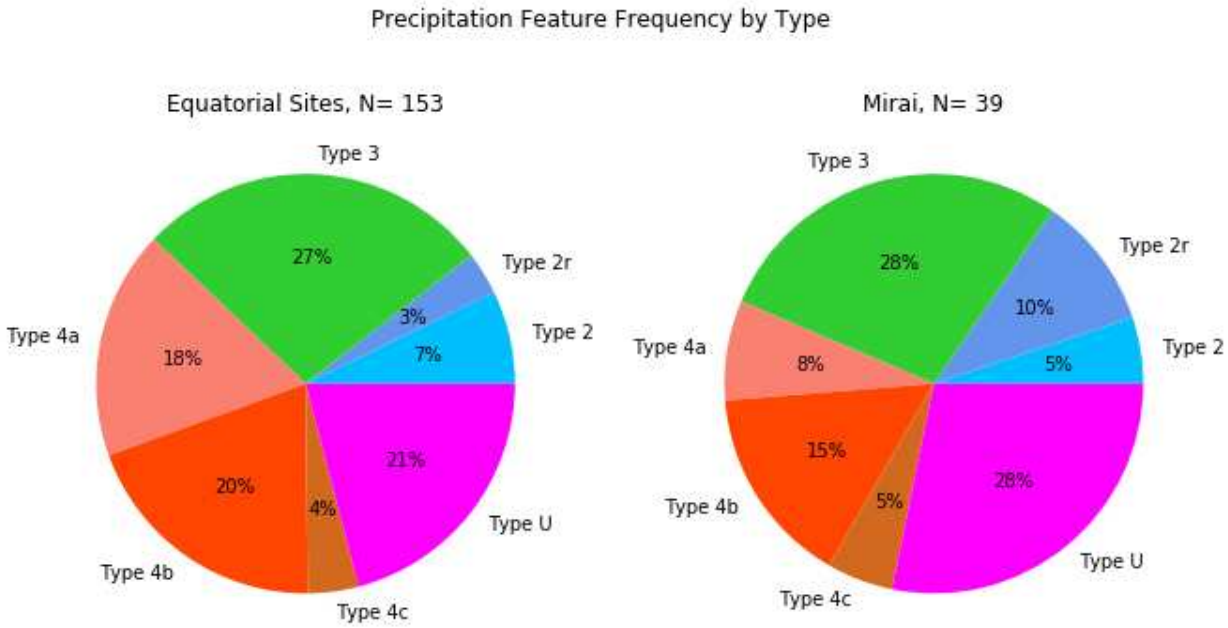

Figure 3.7. Frequency of PF type defined in Figure 3.1 for the equatorial sites and the *Mirai*.

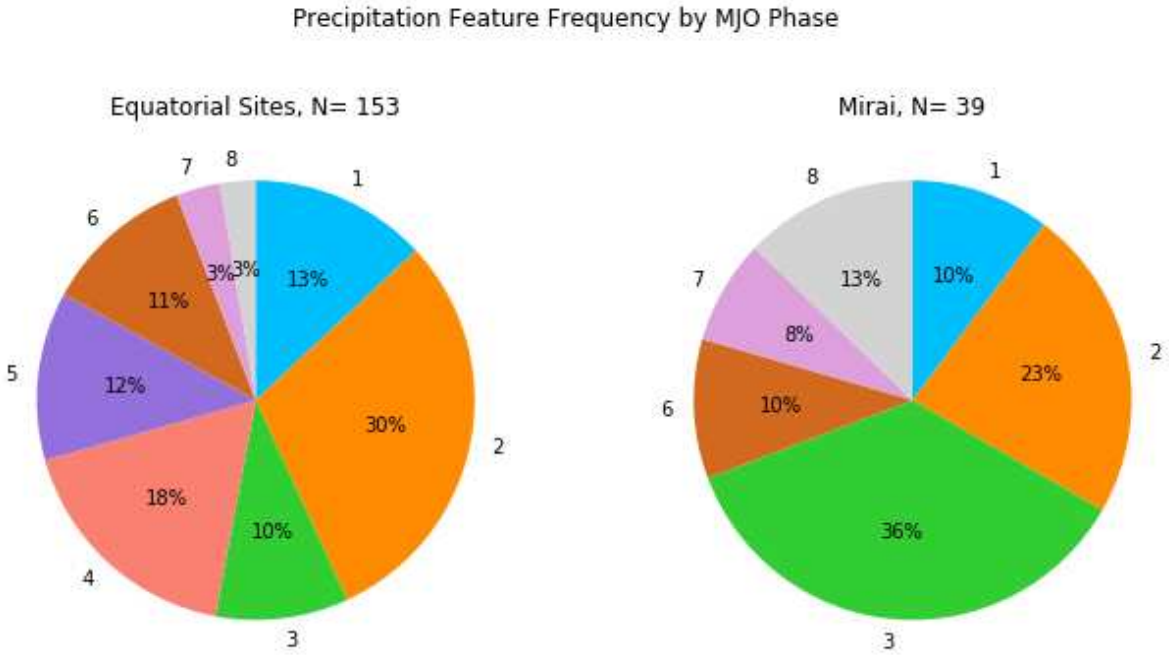

Figure 3.8. PF frequency by MJO phase for equatorial sites and the *Mirai.*

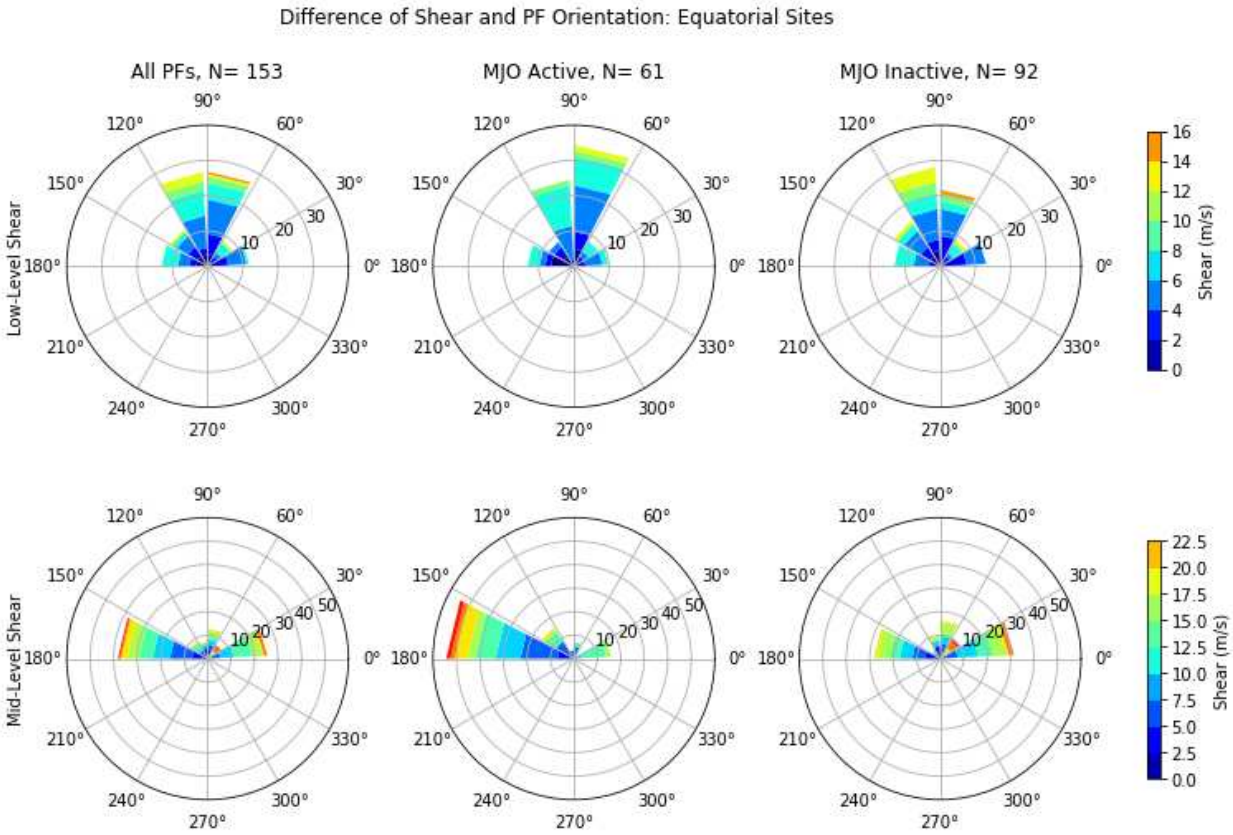

Figure 3.9. Same as Figure 3.6. The first column represents all PFs over every MJO phase. The second column shows only PFs observed during the active phases, and the third column shows PFs observed during the inactive phases. A difference of 90° (±30°) indicates the shear is nearly perpendicular to the PF orientation. A difference of 0° or 180° (±30°) indicates the shear is nearly parallel to the PF orientation. Angles are computed as the smallest angle between the two vectors.

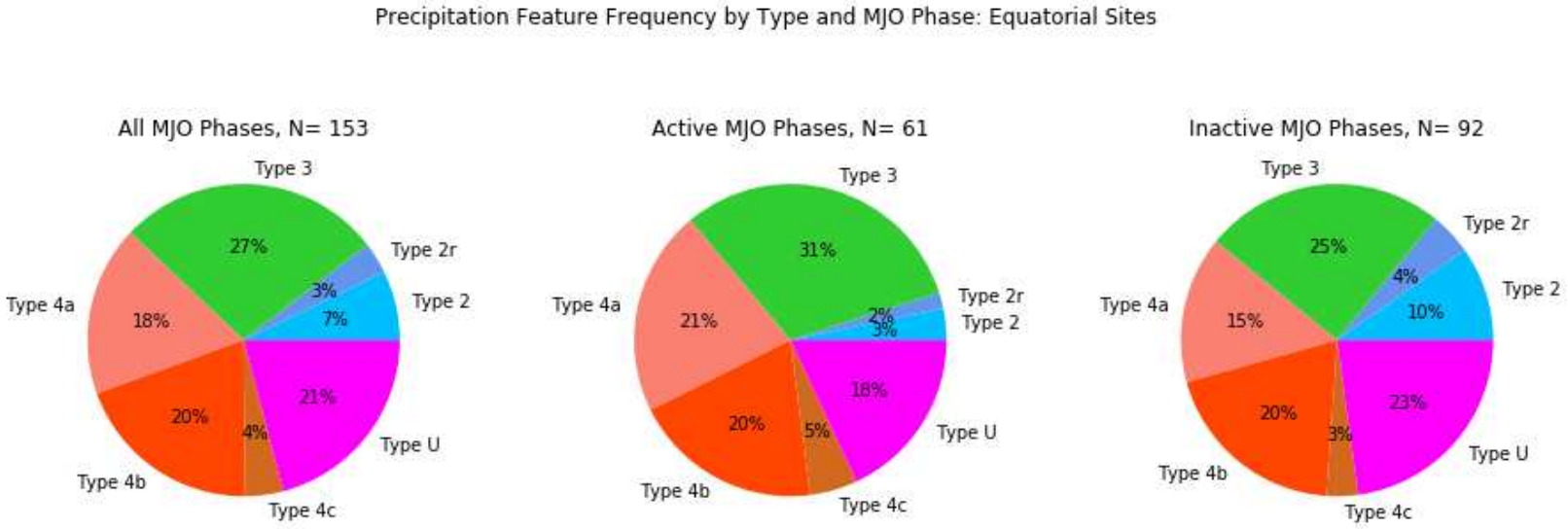

Figure 3.10. Frequency of PF type for equatorial sites during all phases, active phases, and inactive MJO phases.

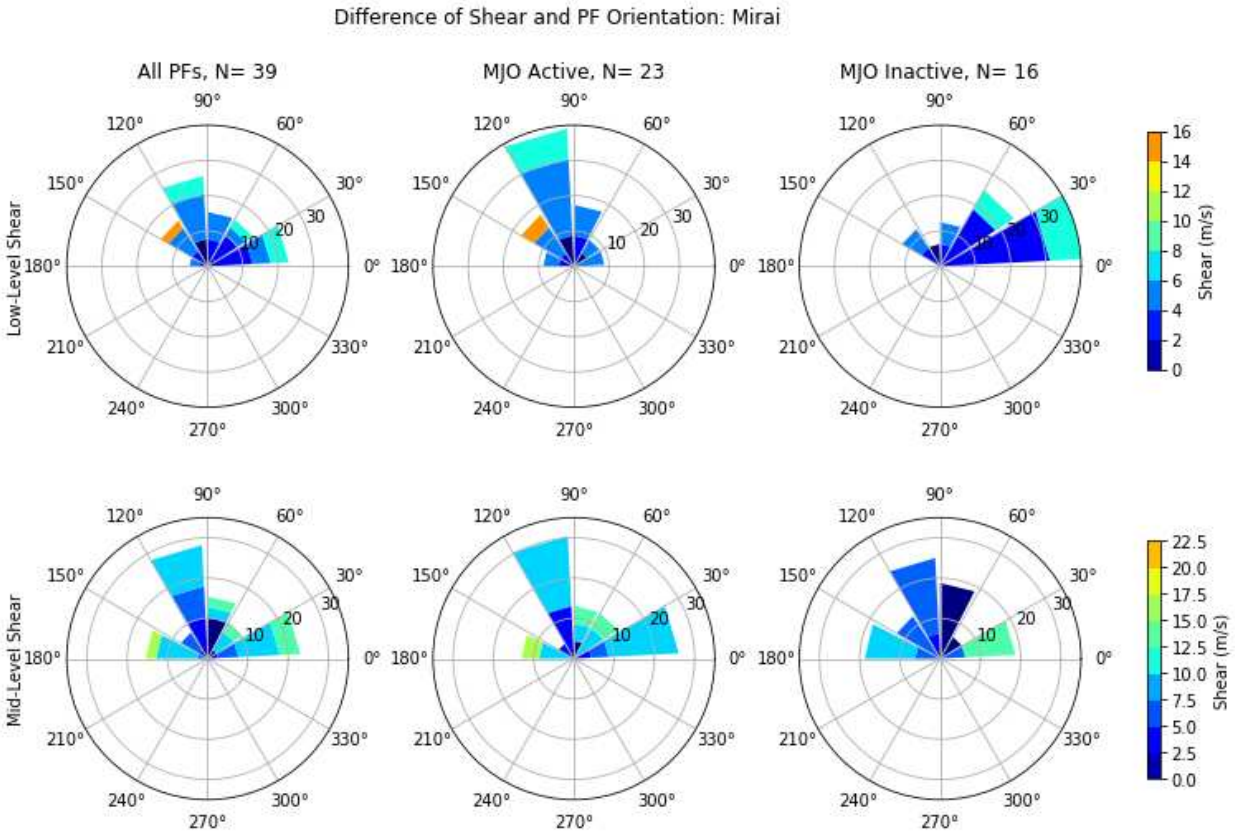

Figure 3.11. Same as Figure 3.9, for the *Mirai* site.

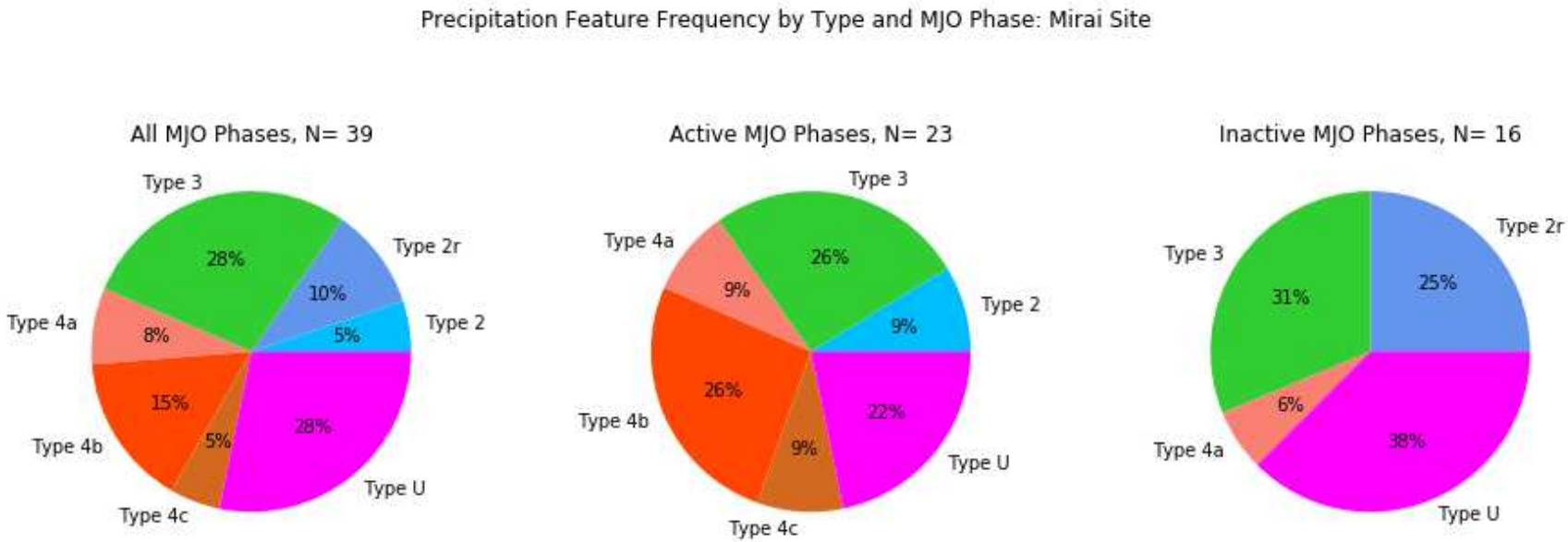

Figure 3.12. Same as Figure 3.10, for the *Mirai* site.

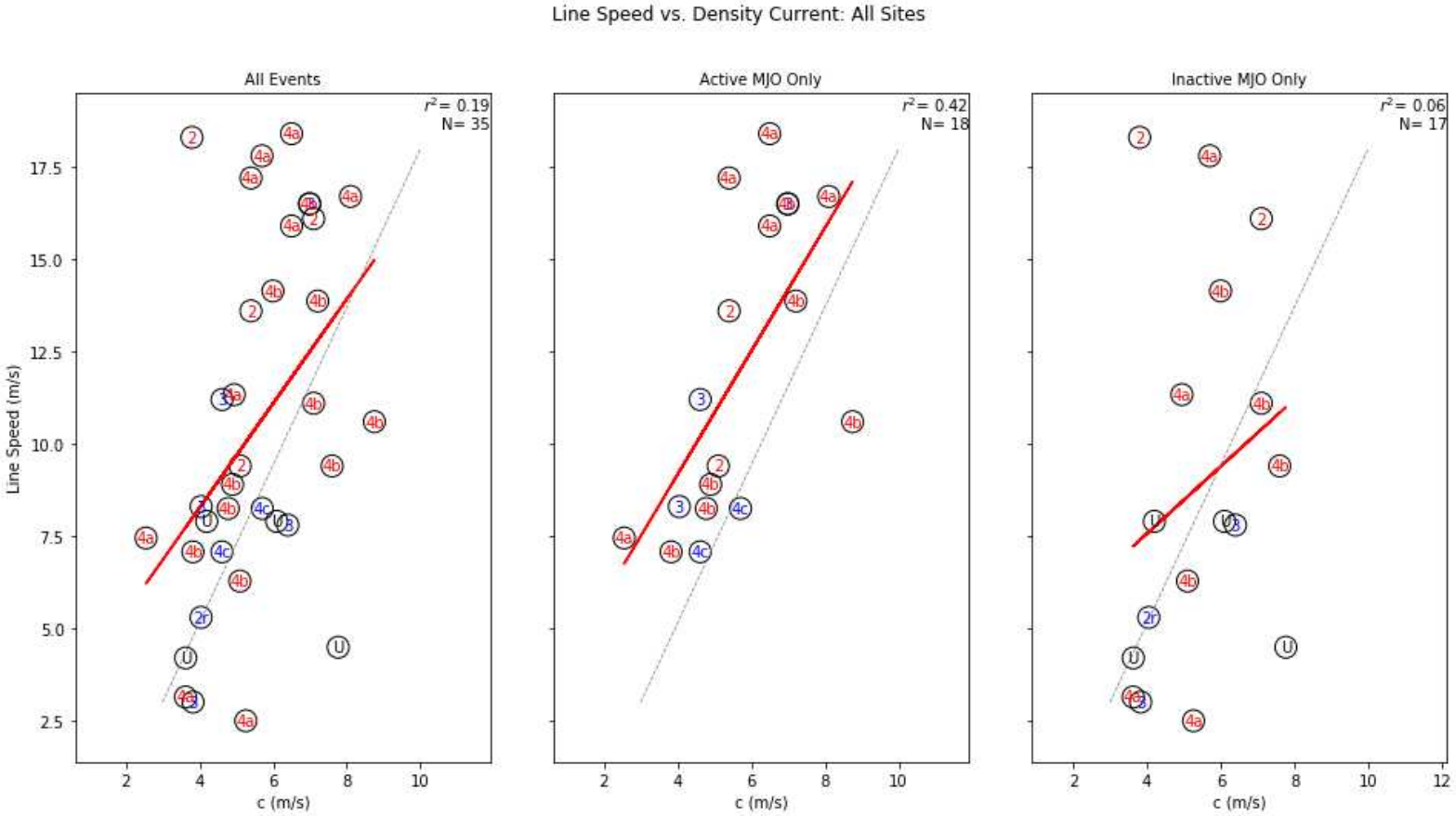

Figure 3.13. PF line speed vs. theoretical density current speed (c) for all sites at all MJO phases, active MJO phases only, and inactive MJO phases only. The grey dashed line represents the ideal situation where c balances the line speed. The red line is a linear regression line. The type (Figure 3.1) of each PF is labeled. More shear-perpendicular PFs are in red (types 2, 4a, 4b). More shear-parallel PFs are in blue (types 2r, 3, 4c). Unclassified PFs are in black.

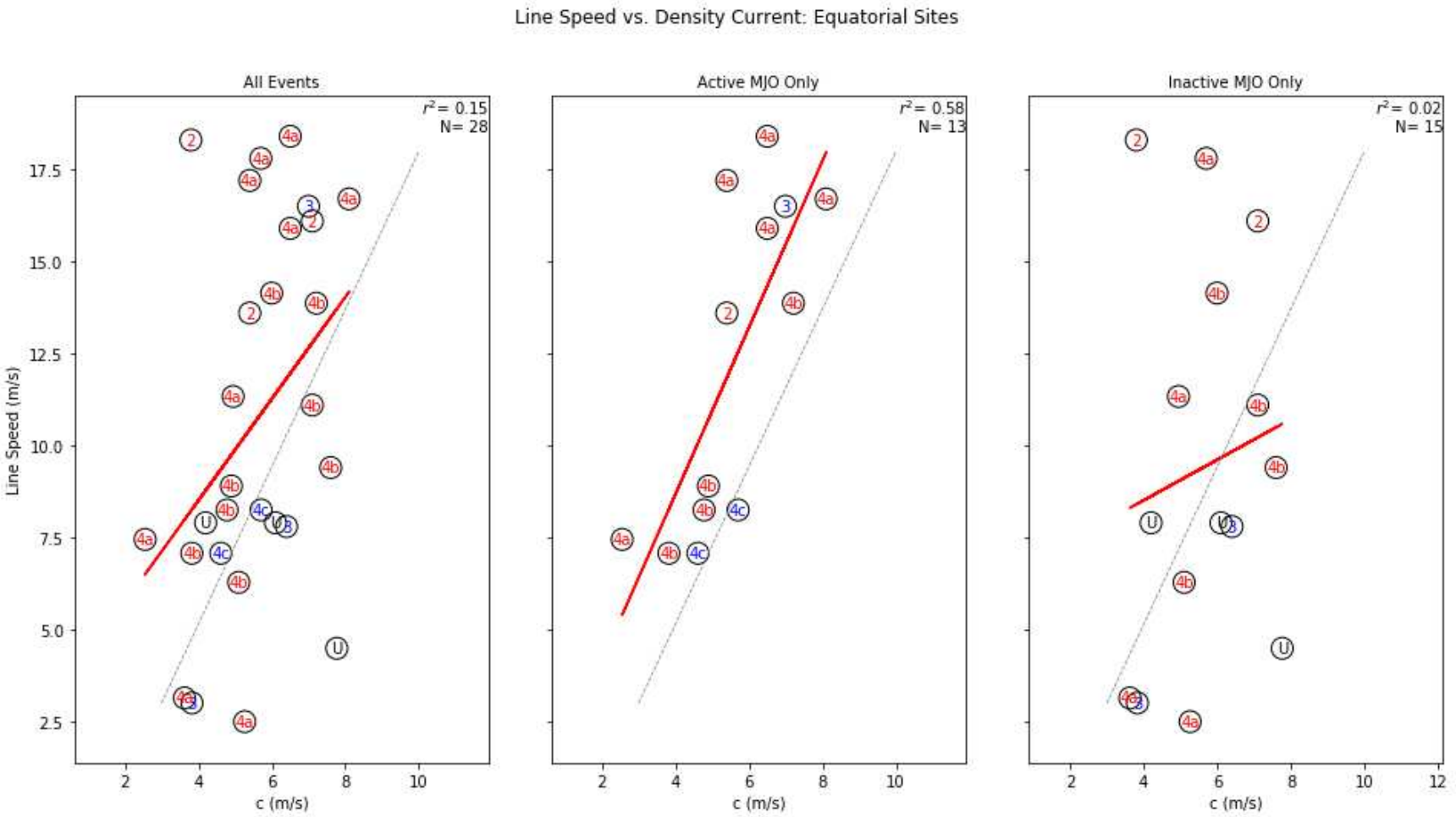

Figure 3.14. Same as Figure 3.13 for the equatorial sites only.

CHAPTER 4: AIR FLOW CHARACTERISTICS WITHIN LINEAR CONVECTIVE SYSTEMS OBSERVED IN DYNAMO

In this chapter, we examine the air flow structures in linear PFs. Figures 4.1 and 4.2 show the archetypical flow features of convective precipitation systems put forth by Moncrieff (1992, hereafter M92) and Kingsmill and Houze (1999, hereafter KH99), respectively. The M92 model is a two dimensional model consisting of a jump updraft, rear overturning inflow current, and an overturning updraft. Its development was based on mass and momentum fluxes in MCSs (M92). KH99 refined the M92 model by applying observations from airborne dual-Doppler radar during TOGA-COARE. Their conceptual model consists of features similar to the M92 model, but includes features that connected inflow from trailing stratiform to the convective core of an advancing squall line. We performed a qualitative examination of the flow features in linear PFs observed in DYNAMO, and compared these to both the M92 and KH99 models of airflow in convective lines accompanied by stratiform precipitation. RHI scans from all three radar sites were examined in detail. Flow features for each model were identified if present.

An example VSR field with annotated flow features from KH99 appears in Figure 4.3b. These features correspond to those in the schematic of KH99 shown in Figure 4.2. The reflectivity field (Figure 4.3a) shows a typical DYNAMO linear PF with a convective core and trailing stratiform approaching the *Revelle* radar. A distinct bright band, behind the leading convective core of 30-50 dBZ, marks the trailing stratiform region. From the VSR field, an updraft inflow (UI) is quite obvious (marked by an upward sloping channel of 10 m s^{-1} velocity away from the radar leading into and through the convective core). A rear

convective updraft outflow (RUO) and weak upper stratiform outflow (USO) was evident exiting the convective core and advancing into the stratiform region. These three features of the KH99 model comprise the 'jump updraft' of the M92 model. The updraft occurs due to unstable environmental air entering the front of the convective line and experiencing a drop in pressure at midlevels. This drop in pressure behind the leading edge is due to the presence of high equivalent potential temperature air aloft. There is an increase in buoyancy, causing a drop in hydrostatic pressure (LeMone 1983). The result is a front to rear upward displacement of air entering the convective line (Houze 2004). A forward convective updraft outflow (FUO) appears as flow entering the convective core (channel of outbound VSR), then exiting aloft in the anvil ahead of the convection (area of VSR returning to the radar). The FUO combined with the UI comprise the 'overturning updraft' of the M92 model. In this case, unstable environmental air enters the front of the convective line as in the case of the jump updraft. Instead of continuing through the line to the rear of the system, it is lofted upwards and ejected back out of the front of the advancing line at upper levels (Houze 2014). A stratiform inflow (SI) (channel of VSR approaching the radar at about 8 m s^{-1}) enters the rear of the convective line. This is also known as a descending rear inflow (Smull and Houze 1985). As low θ_e air enters the rear of an advancing squall line, it is cooled by evaporation of precipitation. This cooling process makes the air less buoyant and causes it to descend (Houze 2014). Although it descends, it does not descend all the way to the surface in this case, so a downdraft outflow (DO) is not identifiable, or at least at the time of this observation. The lack of a DO was not unusual in DYNAMO PFs. Finally, the lower stratiform outflow (LSO) can be seen (red stripe) along

the surface, exiting the rear of the stratiform region. The SI and LSO collectively make up the 'rear overturning current' of the M92 model.

As noted in Chapter 2.7, not all PFs examined in Chapter 3 were available for analysis in this chapter. Overall, twelve cases were identified from the available RHI data acquired during the field campaign. These cases are listed in Table 4.1. All but one of the cases exhibited shear-perpendicular organization. The cases selected for analysis here were all of type 2, 4a, or 4b except for one type 3 PF. Seven of the 12 cases occurred during active MJO phases. Flow features described by M92 and KH99 also appear in Table 4.1. A circle indicates that a PF possessed a feature, a letter 'x' indicates the PF did not possess that feature, and a '?' indicates that it was unclear whether or not a PF possessed that feature. Other characteristics listed in Table 4.1 are the presence of multiple inflow jets and the location of stratiform precipitation, if any (leading, trailing or parallel stratiform). Interestingly, multiple inflow jets were a feature present in five of the PFs. Stratiform precipitation was an important characteristic in the KH99 model. Obviously flow features in trailing stratiform can only be identified if indeed there is stratiform precipitation. In the absence of stratiform precipitation, there are no scatterers for detecting Doppler motions. Leading, trailing, and parallel stratiform linear MCS archetypes are detailed in Parker and Johnson (2004).

The following sections are descriptions of PFs that conform, partially conform, or do not conform to the M92 and KH99 models. Figures 4.4 through 4.15 show RHI and PPI scans for each case. For all radars, PPI scans taken at times just before (top), nearest in time (center), and just after (bottom) the RHI scan time are shown on the right. The black dotted line in the PPI scans is the azimuth at which the RHI was taken. RHI fields are on the

left and are from the same radar at the same time. For the *Revelle* and *Mirai* radars, the RHI fields are comprised of four sub-plots. These plots are: a) reflectivity, b) radial velocity VSR, c) spectral width SW, and d) horizontal divergence as color fill, with reflectivity as contours. Figure 4.4 is one example from the *Mirai*. The NCAR S-Pol radar collected additional, polarimetric fields. In the case of S-Pol, the top three fields (a through c) are the same as in the *Revelle* and *Mirai* radars. The remaining fields are: d) differential reflectivity Z_{DR}, e) co-polar correlation coefficient ρ_{hv}, f) specific differential phase K_{DP}, and g) horizontal divergence as color fill, with reflectivity as contours. Figure 4.5 is one example from S-Pol. All PFs were numbered just as a naming convention and serve no other purpose. For example, 'PF 8' is simply a name used to distinguish it from the rest; the '8' has no meaning other than chronological.

4.1 DESCRIPTIONS OF PFs CONFORMING TO BOTH M92 AND KH99 MODELS

Sections 4.1.1 through 4.1.5 describe PFs that conform to both the M92 and KH99 models. These events contain all of the flow features described in both models. Some features are subtle or questionable, but an argument can be made for their presence.

4.1.1 Mirai PF 72

The *Mirai* PF 72 (Figure 4.4) was a great example of both the M92 model and the KH99 model. This was a type 4b PF that moved away from the radar, from west to east. It was an isolated line of convection with a compact region of trailing stratiform precipitation. The VSR field shows a jump updraft. There is also an overturning updraft and a rear overturning current, making this PF completely conforming to M92. It contains all of the flow features of the KH99 model as well, although the DO is weak. This is one of several PFs that display multiple rear inflow jets. The distinct rear inflow layers are also

identifiable in the SW field as regions of enhanced spectral width, owing to strong vertical shear between the rear inflow and front-to-rear interface. The divergence field for this PF indicates divergence above the primary convective line, with convergence below. There is also an area of convergence on the leading edge of the convective line.

4.1.2 S-POL PF 95

S-Pol PF 95 (Figure 4.5) was a type 4a PF. The reflectivity field indicates a convective band with minimal trailing stratiform. The V_{SR} field shows good agreement with M92, including a jump updraft and rear overturning current. There is evidence of an overturning updraft in the VSR field, but neither the VSR nor SW fields offer concrete support. There are some scatterers moving away from the radar on the leading edge of the convective line. However, due to relative lack of scatterers in the clear air environment ahead of the convection, more complete motion ahead of the precipitation field was not detectable by the radar. This PF had nearly every feature in the KH99 model; the only feature in question was the presence of a FUO (as mentioned above). All other flow features of KH99 were present, including a DO. The SW field offers further evidence of an SI and USO with horizontal stripes of high SW in the stratiform region. These stripes indicate the presence of shear between layers of flow in alternating directions. The divergence field shows divergence above the convective core, and convergence within. There is also a small area of alternating convergence and divergence below 2.5 km in front of the convective line. This corresponds to an area of positive VSR (velocity away from the leading line) and high SW. This combination could be indicative of a gust front.

The additional variables available from the S-Pol polarimetric radar described in Section 2.2 allow us to extract more information from a single RHI. The presence of a

melting layer in the stratiform region is indicated in the Z_{DR} field as a bright band at about 5 km MSL. The actual melting level is a few hundred meters above the bright band. As the melting of oblate ice begins, these particles become coated with water, thereby increasing Z_{DR} (Herzegh and Jameson 1992) and horizontally polarized reflectivity, Z_H. Upon complete melting, particles return to a more spherical shape, reducing Z_{DR} as well as Z_H. Z_{DR} in the convective core increases in areas of high reflectivity, owing to the presence of oblate drops. In this case, there is a marked increase corresponding to reflectivity of 40-50 dBZ. This is an area of more intense rain.

The bright band that appears in the Z_{DR} field is also evident in the ρ_{hv} field. In this case, it appears as a decrease in ρ_{hv}. The melt layer contains precipitation particles that vary in size, shape, and orientation. Since ρ_{hv} decreases in the presence of such a non-uniform distribution of particle size, shape, and orientation (Balakrishnan and Zrnic 1990), the result is a narrow band of decreased ρ_{hv}. Below the melting layer, precipitation particles are all raindrops. These raindrops are similar in shape and size and therefore ρ_{hv} increases to near unity.

There is an area of increased K_{DP} corresponding to the 40-50 dBZ reflectivity core. This increase is indicative of intense precipitation. K_{DP} is not dependent on return power, but is dependent on mass content and mass-weighted oblateness. As a result, there is an increase in K_{DP} where the most intense rain is occurring. Thompson et al. (2018) arrived at a relationship between K_{DP}, Z_{DR}, and rain rate in tropical oceanic environments during DYNAMO. They found that rain rate could be expressed as a function of K_{DP} and Z_{DR}. At S-band that function is:

$$R = 96.57(K_{DP})^{0.80}\,(\xi_{DR})^{-2.11} \qquad (4.1)$$

where R is the rain rate in mmh^{-1}, K_{DP} is in $°km^{-1}$, and ξ_{DR} is the dimensionless linearized differential reflectivity such that

$$10 \log_{10} \xi_{DR} = Z_{DR}.$$

Equation 4.1 is valid for $Z_{DR} > 0.5$ dB and $K_{DP} > 0.3$ $°km^{-1}$ (Thompson et al. 2018). A K_{DP} of about $1°km^{-1}$ and a Z_{DR} of about 1 dB (as observed in Figure 4.8d and 4.8f at a range of about 57 km near the surface) would correspond to an instantaneous rain rate of 59 mmh^{-1}.

4.1.3 S-POL PF 103

S-Pol PF 103 was another type 4a PF and appears in Figure 4.6. Some parallel stratiform was indicated by the PPI scans on the west end of the main convective line. The RHI reflectivity field shows only the convective line with little trailing stratiform. The ρ_{hv} and Z_{DR} fields both show a bright band at about 5 km above the radar. The bright band is considerably more prominent in the ρ_{hv} field. These bands indicate the presence of a melting level and thus some evidence that stratiform processes were taking place behind the convective line. However, this line was decaying along with any stratiform rain. The VSR field shows the presence of all flow features in both the M92 and KH99 models. A jump updraft is clearly visible (denoted by the blue stripe) from the lower right to upper left of the scan. This stripe also represents the UI, USO, and RUO in KH99. Above the jump updraft, there is flow returning back towards the convective region. This is the area of red above the blue stripe and comprises the overturning updraft, or the FUO. The horizontal red stripe behind the jump updraft is the upper leg of the rear overturning current and the SI in KH99. This flow makes it to the surface, and therefore also represents the DO. The horizontal blue stripe at the surface is the lower leg of the rear overturning current and the

LSO. This PF also exhibited multiple rear inflow jets. The SW field supports the presence of a DO and multiple rear inflows, as areas of elevated SW indicate shear between the inflows. The K_{DP} field shows the heaviest precipitation towards the back of the convective core, from about 28 to 30 km from the radar. This is also the area of highest reflectivity. The divergence field again shows divergence above the convective core and convergence below.

4.1.4 S-POL PF 145

Figure 4.7 shows S-Pol PF 145. This type 2 PF had an intense convective line and a compact trailing stratiform region as indicated by the reflectivity field. Evidently, the stratiform region formed as earlier convection dissipated. This PF exhibited all the flow features detailed in M92 and KH99 with the exception of a well-identified SI and rear overturning current. Given the nature of the stratiform precipitation in this case, these flow features were yet to be established. There is some evidence in the VSR and SW fields that an SI did exist. In the VSR field, there are some faint rear inflow streams that could easily have been diluted by imprecise storm motion calculations. The SW field shows multiple inflow jets that appear as horizontal stripes of high SW in the trailing stratiform region on the interface between rear inflow and front to rear flow. Otherwise, the VSR field shows a strong jump updraft and overturning updraft along with the associated UI, FUO, RUO, USO, and LSO. The SW field also depicts the jump updraft. Here, the jump updraft shows up as an area of high SW separating the UI and DO. At roughly 50 km range, there is a vertical channel of high SW that corresponds to the updraft. The Z_{DR} and ρ_{hv} fields indicate a melting layer between 4 and 5 km MSL. The Z_{DR} field also shows an area of large raindrops in the convective core, while the K_{DP} field indicates heavy precipitation in that area as well. For a K_{DP} of about 2°km^{-1} and Z_{DR} of about 2.5 °km^{-1}, Equation 4.1 yields R= 55

mm $^{-1}$. The divergence field remains consistent with the other PFs, showing an area of divergence over convergence in the convective core. It also shows some divergence ahead of the line, where the overturning updraft was moving away from the jump updraft.

4.1.5 S-POL PF 148

S-Pol PF 148 also displayed all flow features from both models and appears in Figure 4.8. The reflectivity field shows a convective core of over 40 dBZ with trailing stratiform precipitation. The VSR field indicates a descending SI and associated DO. An LSO completes the rear overturning current. The presence of a UI, RSO, and USO comprise the jump updraft. An FUO was also present and comprised the overturning updraft. This PF contained multiple rear inflow jets as indicated by the VSR and SW fields. A bright band was clearly evident in the Z_{DR}, ρ_{hv}, and K_{DP} fields at just below 5 km MSL. An area of elevated K_{DP} indicates intense precipitation in the convective core near 75 km from the radar. The divergence field shows divergence above the convective core and convergence below. There is also an area of strong convergence at the leading edge of the line where the SI meets the UI.

4.2 DESCRIPTION OF PFs CONFORMING ONLY TO M92 MODEL

Sections 4.2.1 through 4.2.5 describe PFs that conform to only the simpler M92 model. These PFs may still exhibit some features in the KH99 model, but some are notably absent.

4.2.1 REVELLE PF 23

Revelle PF 23 is depicted in Figure 4.9. This PF was moving towards the radar from ESE to WNW. It was a type 4b PF. The reflectivity field shows a convective core with some dissipating cells behind it, which formed a trailing stratiform precipitation zone. The VSR

field shows all of the features in the M92 momentum transport model. These features are a jump updraft, a rear overturning current, and an overturning updraft. The VSR field shows a UI, FUO, and RUO in the convective core. In the stratiform region, there is a USO aloft, an SI entering near the top of stratiform precipitation, and an LSO along the surface. A DO is notably absent in this PF, but that is all that was missing in order to conform to the KH99 model. The horizontal flow features are all visible in the SW field as bands of elevated SW separating the inbound flow layers from the outbound flow layers. This is one of several PFs that contained multiple inflow jets. These are visible in both the VSR and SW fields. On the VSR field, note the two blue horizontal stripes of about -5 m s^{-1}. In the divergence field, we again see divergence above the convective core (at about 22 km) with convergence along the front of the line. There is also some weaker convergence in the lower part of the convective core, near the surface.

4.2.2 REVELLE PF 32

Figure 4.10 shows the *Revelle* PF 32, another type 4b. PF 32 was approaching the radar moving east to west. The reflectivity field shows a convective core with trailing stratiform precipitation. This is an excellent example of the M92 model, and was also used as an example in Figure 4.3. A jump updraft is clearly visible in the VSR field as a region of high spectral width that angles from lower left to upper right between 30 and 40 km range. Ahead and aloft of the jump updraft, the area of about -10 ms^{-1} indicates flow returning towards the radar. This is indicative of an overturning updraft. Behind the jump updraft, there is another area of -5 to -10 m s-1 that indicates airflow towards the radar, with a thin area of about 5 m s^{-1} near the surface, indicating flow away from the radar. Together, these features form the rear overturning current. This PF also conformed well to the KH99

model. The VSR field shows a UI, FUO, and RUO in and near the convective core. Behind the convective core, in the stratiform region, the SI and LSO form the rear overturning current described by M92. The USO is weak, but there is evidence of airflow away from the radar above the SI. Also questionable is the presence of a DO. There is some evidence of a nose of sinking air at a range of about 40 km, but it is difficult to determine if this feature reached the surface. The divergence field shows convergence where the SI merges with the UI, and divergence along the interface of the FUO and the UI. There is also divergence above the convective core.

4.2.3 S-POL PF 20

S-Pol PF 20 (Figure 4.11), a type 4a PF, was a narrow band without trailing stratiform precipitation. The reflectivity field indicates intense precipitation in the core of the convective line with an area greater than 50 dBZ present at about 24 km range. There was some leading stratiform, probably due to the LL downshear propagation and ML shear-parallel organization. The VSR field indicates strong agreement with the M92 model, showing a jump updraft, overturning updraft, and rear overturning current. The jump updraft is also supported in the SW field, denoted by an area of high SW that separates the UI from the SI. There is a small area of low SW at about 23 km surrounded by increased SW at the boundary of the updraft, likely due to high turbulence as convective updrafts and downdrafts merge. This PF also fared well in the KH99 model. Visible in the VSR field are a UI, FUO, SI, DO, and LSO. However, this PF lacked a USO and RUO as the jump updraft did not continue through to the rear of the system. The Z_{DR} and ρ_{hv} fields show a bright band at about 4 km MSL. This bright band is again the location of the melting level. An increase in Z_{DR} and K_{DP}, along with a decrease in ρ_{hv}, at about 24 km range indicates the presence of

intense rainfall indicated by the reflectivity field. The decrease in ρ_{hv} may be due to a broadening of the drop size distribution by the increase in turbulence (as indicated by the increase in SW). Finally, the divergence field shows an area of divergence where the overturning updraft separated from the jump updraft. There is also an area of divergence above the convective core. There is an area of convergence inside and behind the convective core, where the descending rear inflow meets the jump updraft.

4.2.4 S-POL PF 146

Figure 4.12 shows S-Pol PF 146. The reflectivity field indicates a 50 dBZ convective core with some trailing stratiform precipitation. The VSR field shows all flow features from both models with the exception of a well-defined DO. The SI feature started to descend in the convective core but failed to reach the surface. Otherwise, the VSR field depicts an SI and LSO, constituting the rear overturning current. There is a UI, RUO, and USO. These make up the jump updraft of M92. The FUO is rather subtle but present, and, along with the UI, formed the overturning updraft. In this case, the SW field supports the presence of flow features observed in the VSR field quite well. The areas of high SW (4-5 m s^{-1}) indicate turbulence at the interface of inflows and outflows. For example, the line of high SW from about 73 km sloping upwards to about 57 km is the interface between the UI and the SI. The more horizontal stripe of high SW from about 70 km going back towards the radar is the interface between the SI and the LSO. This feature of the SW field clearly shows the SI descending as this rear inflow approaches the convective core. The SW field also shows the separation of the FUO from the UI as a steeper area of high SW towards the front of the convective line. The Z_{DR} and ρ_{hv} fields identify the melting layer between 4 and 5 km MSL. The K_{DP} field indicates heavy precipitation of about 70 mm h^{-1} in the area of the highest

reflectivity Thompson et al. 2018). Finally, the divergence field indicates divergence above and convergence inside the convective core.

4.3 DESCRIPTIONS OF PFs NOT CONFORMING TO EITHER MODEL

Sections 4.3.1 through 4.3.3 describe PFs that do not conform to either model. These PFs may still exhibit some features from each model.

4.3.1 REVELLE PF 8

Figure 4.13 shows PF 8 from the *Revelle* radar. This PF moved towards the radar when the RHI scan was taken. It was an isolated band but showed some leading stratiform echo. It was a type 2 PF, exhibiting strong LL shear perpendicular to the convective line and weak ML shear. In examining the VSR field, this particular PF does not fit into the M92 model very well. It showed some evidence of a rear overturning current but only a questionable jump updraft and no overturning updraft. In the KH99 model, it showed some features associated with the M92 rear overturning current, such as SI and an LSO. A USO and RUO were also visible. However, there was a lack of any DO that extended all the way down to the surface. There was also no evidence of an FUO and only a hint of an UI. The SW field showed an area of low SW in the area of the USO with an increase SW above and below it, indicating turbulence along the boundary of the outflow. There was also a high SW band at the interface of the SI and UI. The divergence field shows areas of convergence at the top of the convective core and divergence above it, suggesting strong lift in the area of greatest reflectivity.

4.3.2 REVELLE PF 77

Figure 4.14 shows *Revelle* PF 77. This was a type 3 PF, having strong parallel ML shear and weak LL shear. This one did not show strong adherence to either M92 or KH99.

Although a jump updraft is visible in the VSR field, there was no overturning flow ahead of or behind the jump updraft. The VSR field did not reveal an LSO, DO, or FUO. Features present from the KH99 model were only a UI, USO, RUO, and a weak SI. The interface between the UI and SI are visible in the SW field as a stripe of elevated SW (3-4 m s^{-1}) behind the convective core. The divergence field shows some weak low-level convergence in the convective core and divergence aloft.

4.3.3 REVELLE PF 81

Revelle PF 81 (Figure 4.15) was a type 4b PF and similar in structure to PF 77. Again, this PF did not follow M92 or KH99. Like PF 77, PF 81 has a jump updraft visible in the VSR field. However, there was a lack of a rear overturning current and an overturning updraft. Some KH99 flow features were present. The VSR field shows a UI, USO, RUO, SI, and DO. The SW field shows a stripe of high SW between the USO and SI, and near the front of the convective line between the UI and SI. There does not appear to be a FUO or LSO. The reflectivity field indicated a rearward slanted convective line with some trailing stratiform precipitation. The divergence field indicated divergent flow above the leading convection, and convergence in the convective core. One problem with this particular PF was that the RHI was not taken at an ideal angle as the cross section passed through part of a trailing band of convection instead of the trailing stratiform region. Thus flows in the stratiform region could not be identified very well.

4.4 SYNTHESIS

In this chapter, we examined twelve DYNAMO PFs for which there was detailed RHI and PPI radar data. Due to the sampling difficulties detailed in Chapter 2.7, the sample size was limited to these features. However, despite the difficulties in obtaining PFs across all

MJO phases and PF types, some qualitative conclusions can still be drawn from the available events. Flow features common to all of the PFs examined were a UI and SI, or a jump updraft and descending rear inflow. These features were questionable in two events, yet identified in the remaining ten. The absence of a DO was the most common shortcoming in features that did not conform to the KH99 model. The absence of an FUO was the next most common shortcoming. The presence of trailing stratiform was an important factor of whether or not a PF fit the KH99 and M92 models. The PF type was a determining factor in whether or not trailing stratiform was present. The divergence signature was consistent across all PFs and indicated divergence above a convective core with convergence below. The polarimetric fields along with SW were helpful in identifying boundaries between flow features and diagnosing precipitation processes. Finally, multiple inflow jets were present in five of the twelve PFs.

Of the twelve PFs analyzed, five fit both the KH99 and M92 models, while an additional four PFs fit the M92 model, for a total of nine PFs fitting one or the other. Only three fit neither conceptual model, but each of these three exhibited features of M92, KH99, or both. This speaks to the validity of both models. Despite these three events, all events exhibited at least a jump updraft and descending rear inflow. These two persistent features act to (1) transport front to rear horizontal momentum from low levels to mid and upper levels behind the convective line, and (2) transport rear to front horizontal momentum from mid and upper levels to lower levels (LeMone et al. 1984). The lack of or the presence of a DO was the downfall of six PFs. In their modeling study of downshear-propagating tropical MCSs, Moncrieff and Lane (2015) found that a mesoscale downdraft was not always present. Although our results do not support the full findings of Moncrieff

and Lane (2015), they certainly suggest that the presence of a DO in the KH99 model warrants further investigation. The absence of an FUO was the next most common shortcoming in the KH99 model. A clear environment ahead of a convective line, void of any precipitation, can explain this problem. Because the FUO exists out in front of an MCS, there may not be ample scatterers for the radar to detect motion in this part of the PF.

The presence of trailing stratiform precipitation was an important factor in whether or not a PF conformed to the KH99 model. Of the PFs that conformed to both models, only one lacked trailing stratiform (S-Pol PF 103). PF type played a role in whether trailing stratiform was present. PF types that lacked strong ML parallel shear (2 and 4b) were more likely to have trailing stratiform, implying that hydrometeors were carried rearward by the front to rear flow (Rutledge and Houze, 1987).

The SW field provided useful insight in identifying the boundaries between flow features while the polarimetric fields provided insight regarding microphysical processes. Areas of increased SW indicated turbulent interfaces between channels of air flowing in different directions. These interfaces were consistently present between the SI and USO. In some cases, vertically oriented areas of high SW indicated the presence of an updraft. The polarimetric fields of Z_{DR} and ρ_{hv} indicated the location of a melting layer in the stratiform area if one was present. Variations in drop size distribution could be gleaned from the ρ_{hv} field. An instantaneous rain rate was calculated for some PFs using a function of K_{DP} and Z_{DR} (Equation 4.1).

One feature common to five of the twelve PFs that warrants further investigation is the presence of multiple rear inflow jets. S-Pol PF 148 and *Mirai* PF 72 are excellent

examples of this phenomenon (Figures 4.4 and 4.8). They both show multiple, descending inflows. This phenomenon had not been previously documented in the literature.

Table 4.1. List of PFs analyzed in Chapter 4. The fields are the radar site, PF identifying number, PF type (from **Figure 3.1**), MJO Phase, presence of flow features from KH99 (from **Figure 4.2**), presence of flow features from M92 (from **Figure 4.1**), presence of multiple rear inflow jets, and the location of stratiform precipitation (if any). A 'o' indicates a feature is present, 'x' indicates a feature is not present, and '?' indicates that it is not clear whether a feature is present or not. 'TS' indicates trailing stratiform, 'LS' indicates leading stratiform, and 'PS' indicates parallel stratiform.

				Kingsmill and Houze (1999)							Moncrieff (1992)				
Site	PF	Type	MJO Phase	RUO	FUO	UI	USO	SI	LSO	DO	Rear Overturning current	Jump Updraft	Overturning Updraft	Multiple inflow?	Stratiform Precip?
Mirai	72	4b	3	o	o	o	o	o	o	?	o	o	o	o	TS
S-Pol	95	4a	3	o	?	o	o	o	o	o	o	o	?		TS
S-Pol	103	4a	3	o	o	o	o	o	o	o	o	o	o	o	some PS
S-Pol	145	2	5	o	o	o	o	?	o	o	?	o	o	o	TS
S-Pol	148	4a	5	o	o	o	o	o	o	o	o	o	o	o	TS
Revelle	23	4b	2	o	o	o	o	o	o	x	o	o	o	o	LS
Revelle	32	4b	2	o	o	o	?	o	o	?	o	o	o		TS
S-Pol	20	4a	1	x	o	o	x	o	o	o	o	o	o		none- isolated band
S-Pol	146	2	5	o	o	o	o	o	o	x	o	o	o		TS
Revelle	8	2	6	o	x	?	o	o	o	x	o	?	x		none- isolated band
Revelle	77	3	3	o	x	o	o	o	x	?	x	o	x		PS and some TS
Revelle	81	4b	3	o	x	o	o	o	x	o	x	o	x		TS

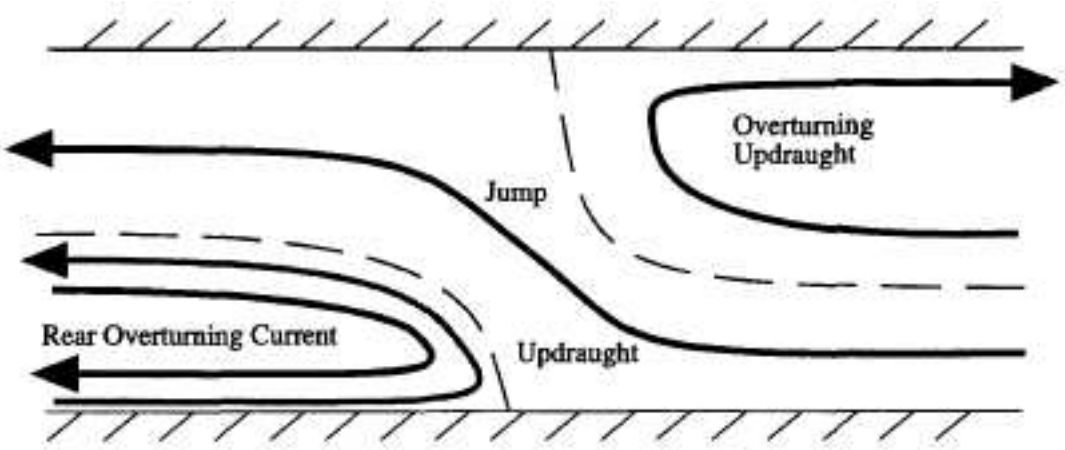

Figure 4.1. Schematic of the Moncrieff (1992) model of momentum transport in a convective system. Flow features are the rear overturning current, jump updraft, and overturning updraft. From Kingsmill and Houze (1999).

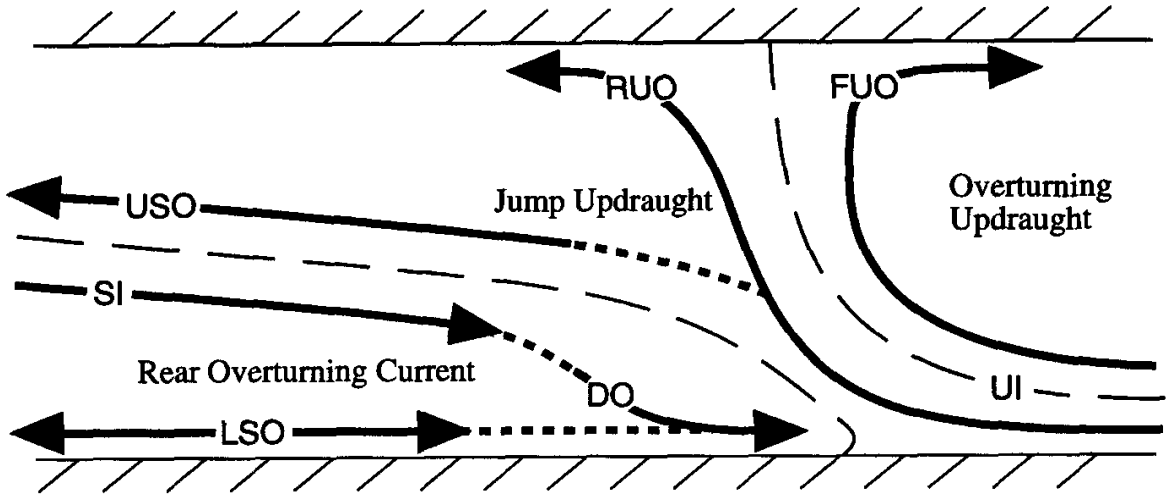

Figure 4.2. Schematic of Kingsmill and Houze's (1999) modified version of Moncrieff's (1992) momentum transport model. Flow features are the lower stratiform outflow (LSO), stratiform inflow (SI), upper stratiform outflow (USO), downdraught outflow (DO), rear convective updraft outflow (RUO), forward convective updraft outflow (FUO), and convective updraft inflow (UI). From Kingsmill and Houze (1999).

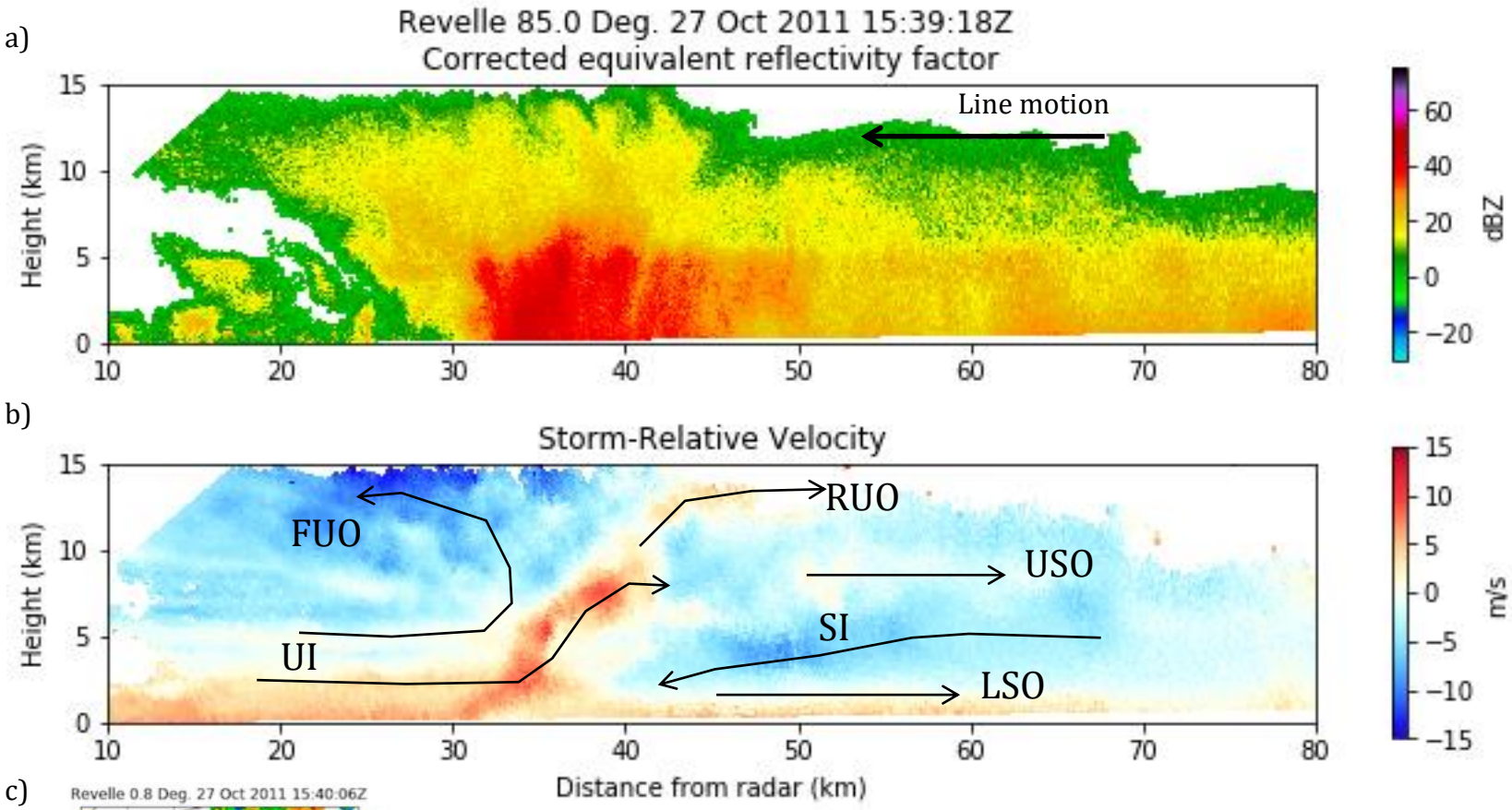

Figure 4.3. An example of the KH99 model flow features defined in Figure 4.2 on an RHI from DYNAMO. This PF is moving towards the *Revelle* radar, from east to west. a) Reflectivity field showing leading convective line with trailing stratiform, b) VSR field with flow features from KH99 annotated, and c) A PPI scan at the time of the RHI. The black dashed line on the PPI is along the azimuth of the RHI scan (85°). The lack of a downdraft outflow (DO) was common in DYNAMO PFs.

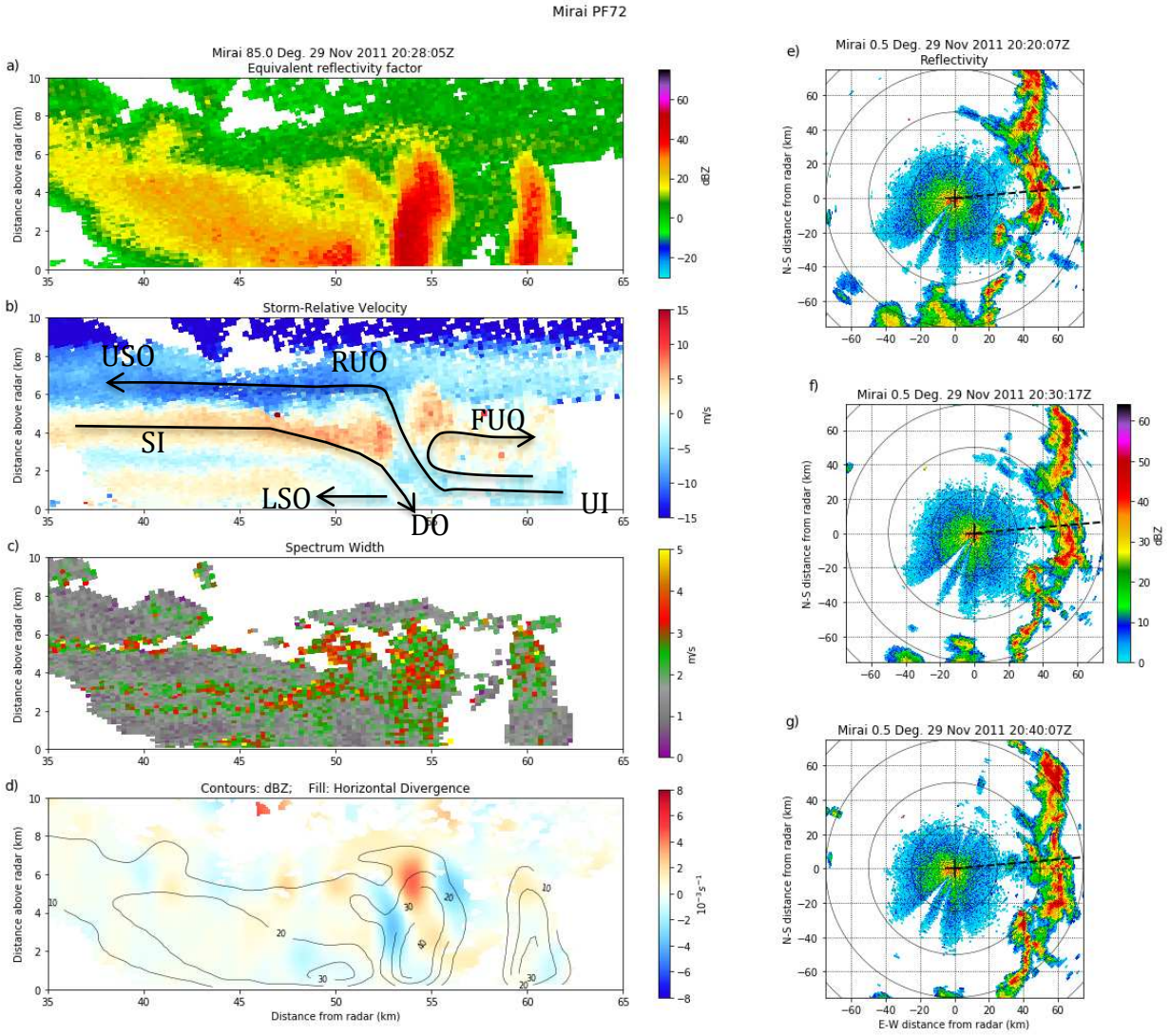

Figure 4.4. *Mirai* radar, PF 72. This PF was moving away from the radar from west to east. a) Reflectivity, b) Storm-relative velocity, c) Spectrum width, and d) Horizontal divergence in color fill with reflectivity in contours. PPI scans of reflectivity are on the right. From top to bottom: e) Scan just before the RHI scan, f) Nearest in time to the RHI scan, and g) Just after the RHI scan. The dashed black line represents the azimuth at which the radar was pointed during the RHI. In this case, it was 85°.

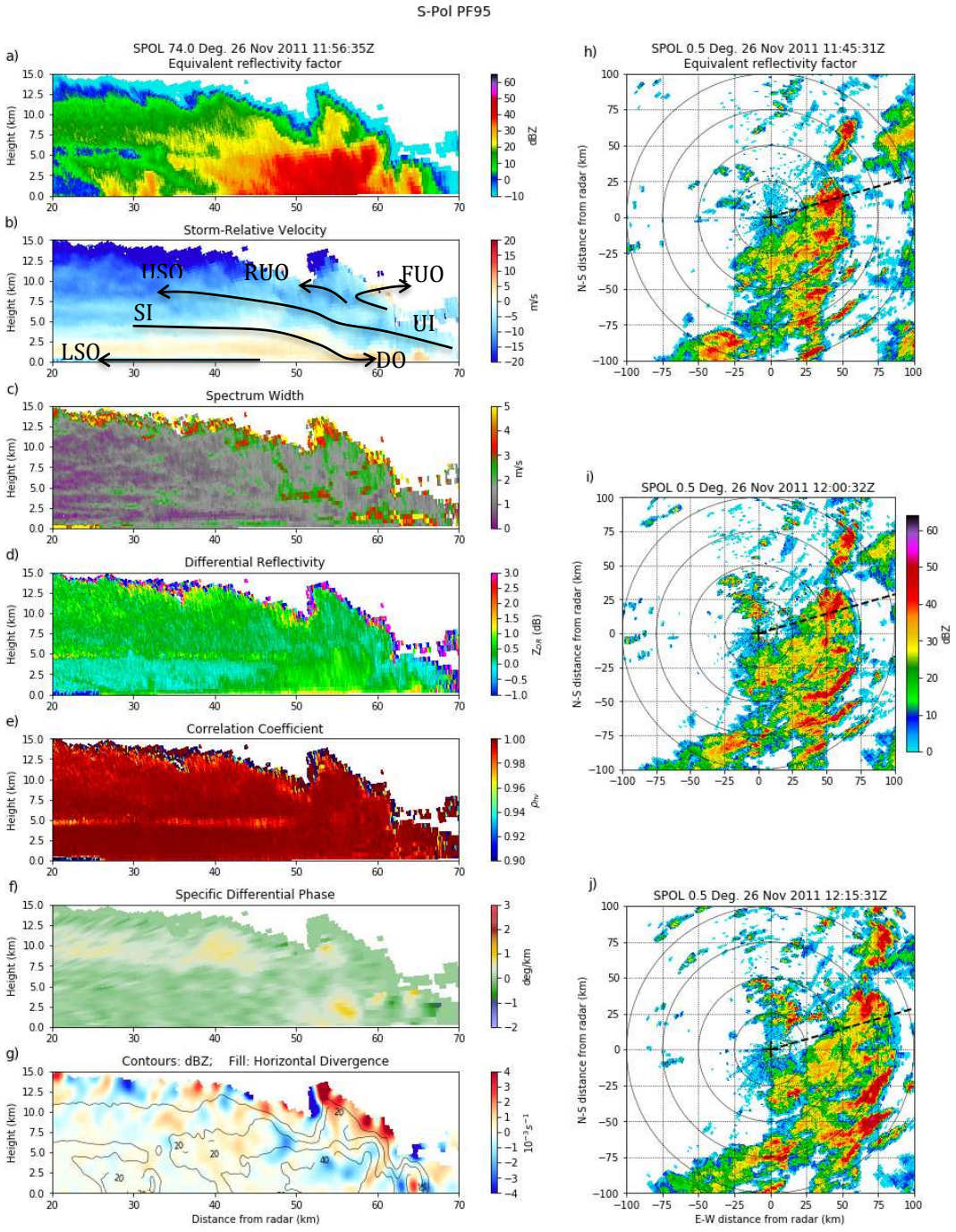

Figure 4.5. S-Pol radar, PF 95. This PF was moving away from the radar from west to east. a) Reflectivity, b) Storm-relative velocity, c) Spectrum width, and d) Differential reflectivity (Z_{DR}), e) Correlation coefficient (ρ_{hv}), h) Specific differential phase (K_{DP}), and g) Horizontal divergence in color fill with reflectivity in contours. PPI scans of reflectivity are on the right. From top to bottom: h) Scan just before the RHI scan, i) Nearest in time to the RHI scan, and j) Just after the RHI scan. The dashed black line represents the azimuth at which the radar was pointed during the RHI scan. In this case, it was 74°.

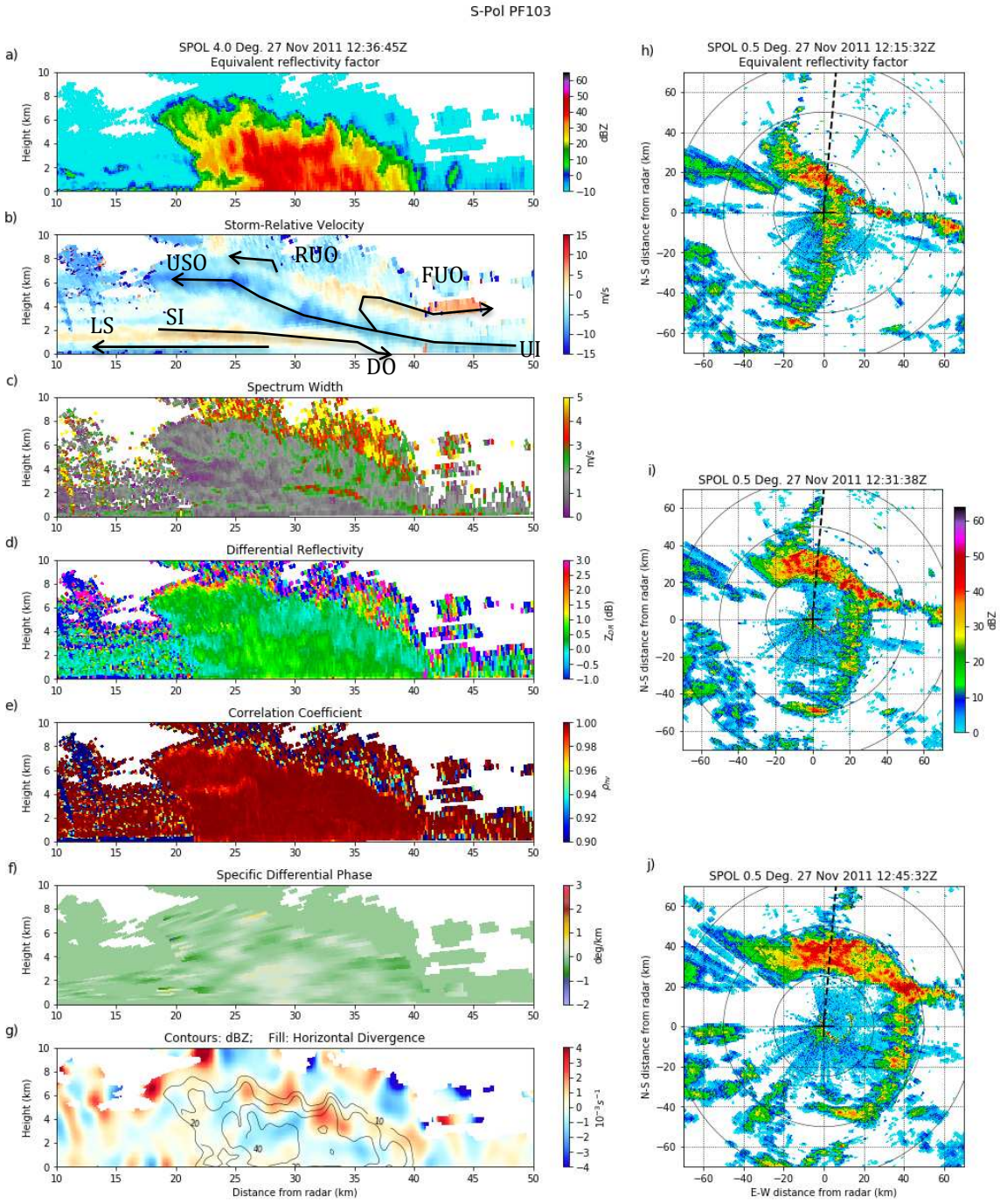

Figure 4.6. Same as Figure 4.5 but showing S-Pol radar PF 103. This PF was moving away from the radar from south to north.

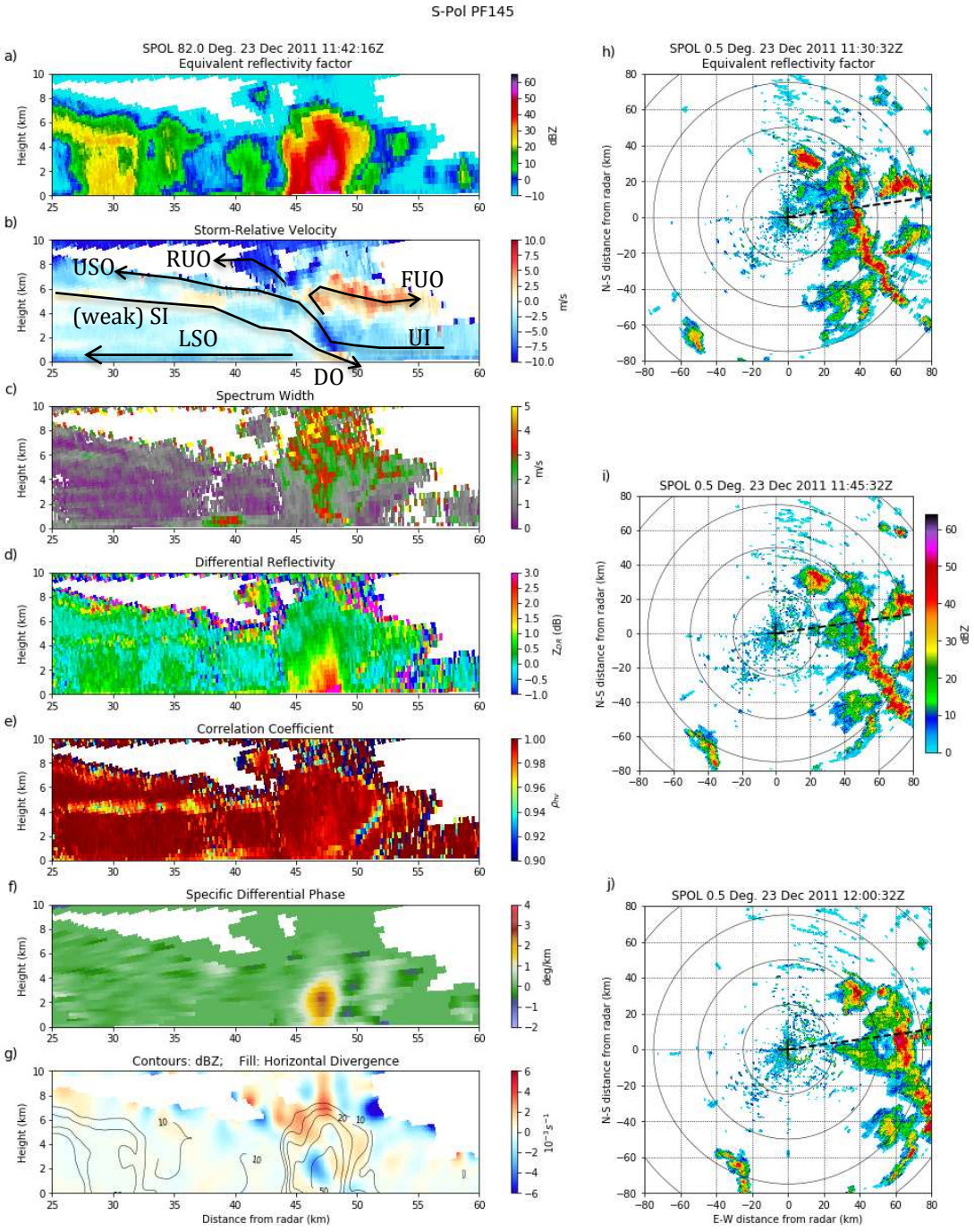

Figure 4.7. Same as Figure 4.5 but showing S-Pol radar PF 145. This PF was moving away from the radar from west to east.

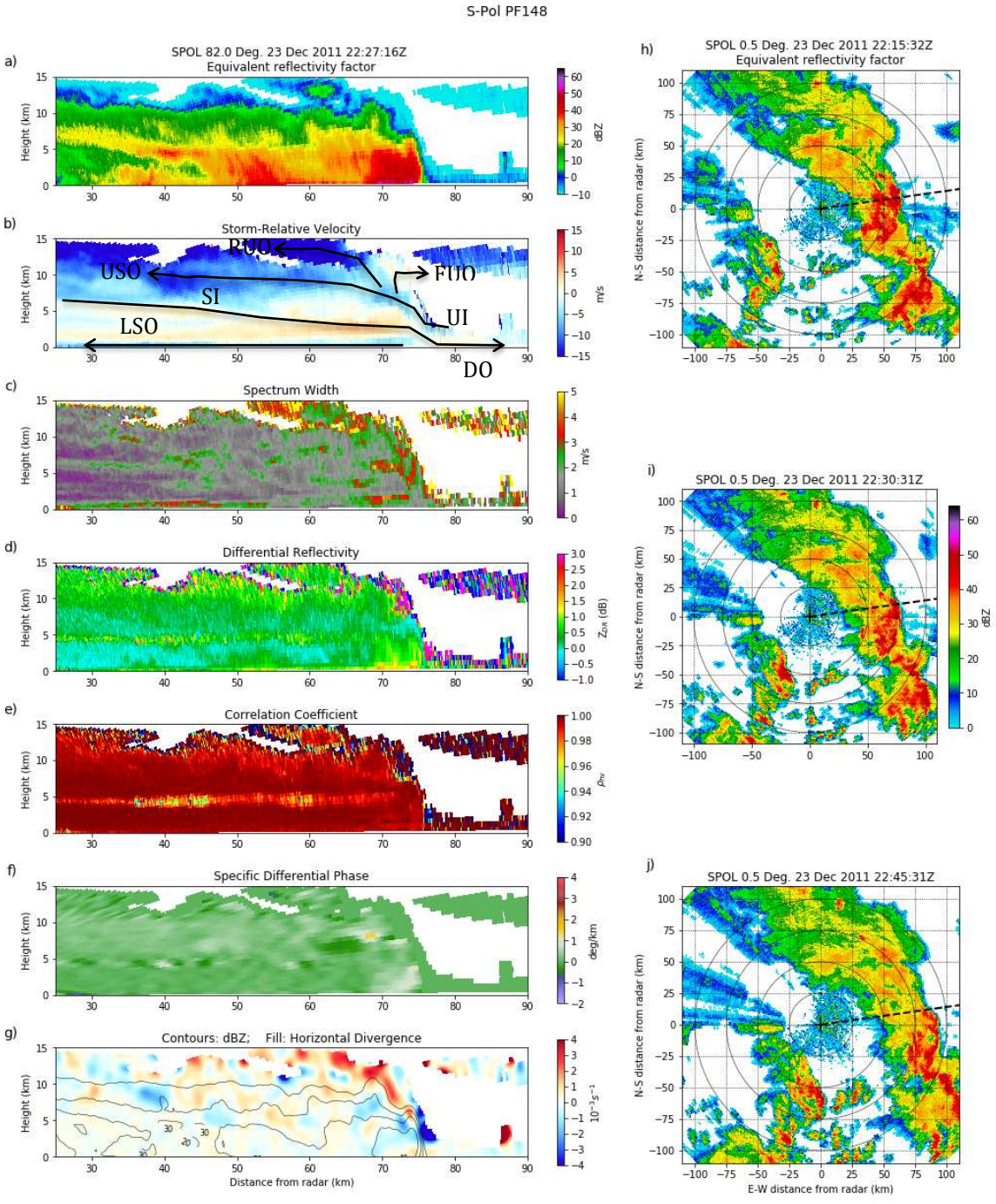

Figure 4.8. Same as Figure 4.5 but showing S-Pol radar PF 148. This PF was moving away from the radar from west to east.

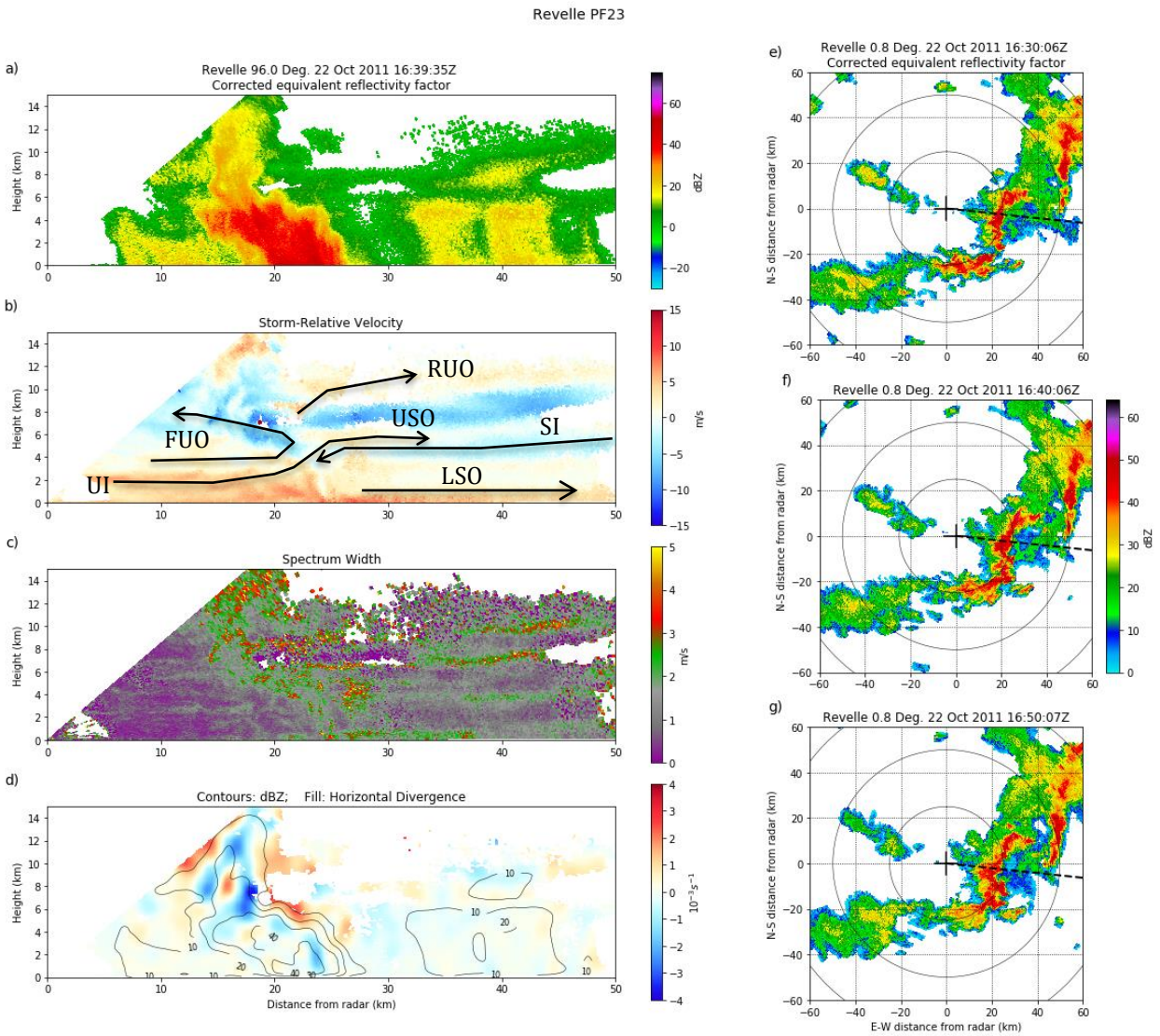

Figure 4.9. Same as Figure 4.4 but showing *Revelle* radar PF 23. This PF was moving towards the radar from ESE to WNW.

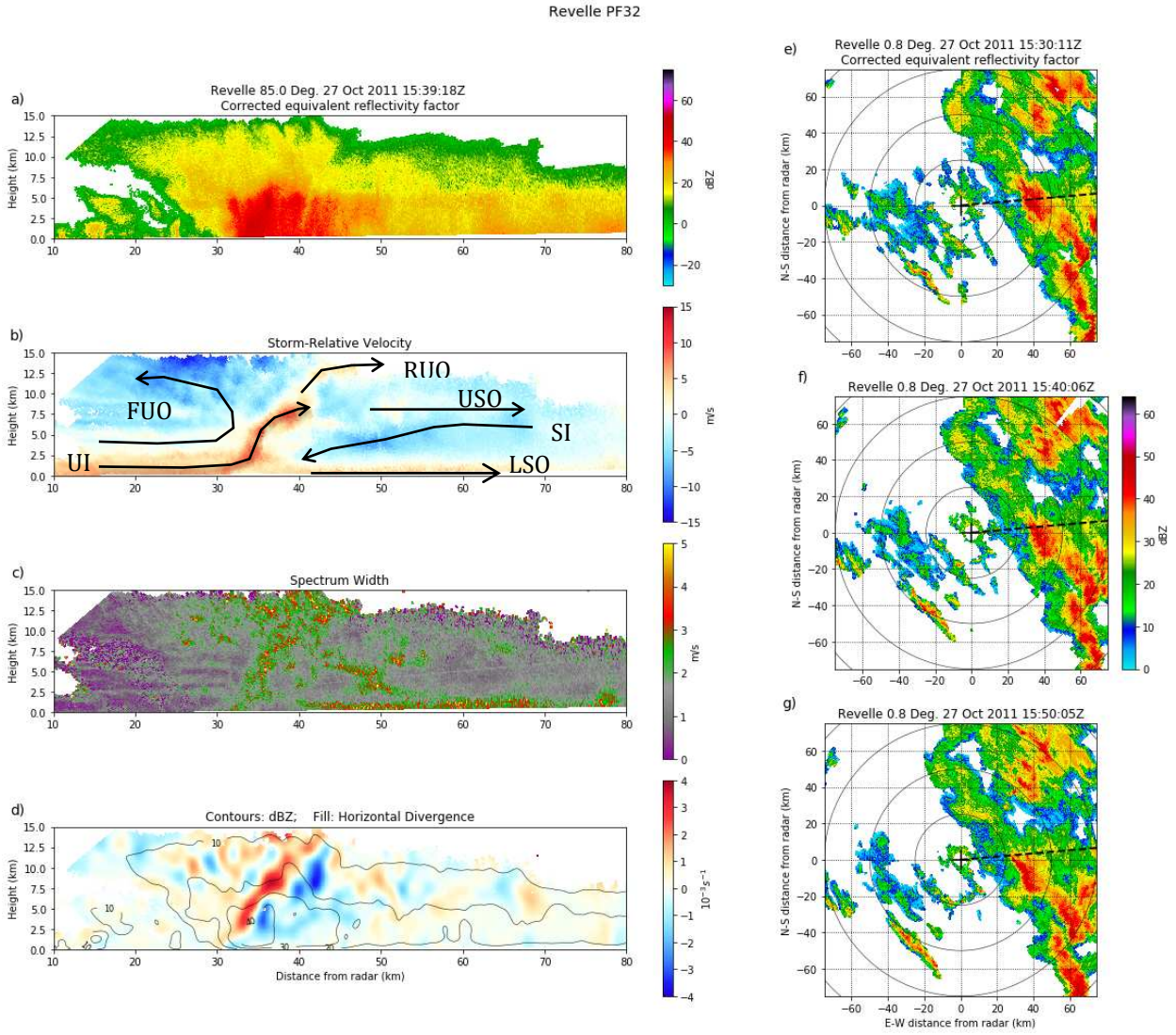

Figure 4.10. Same as Figure 4.4 but showing *Revelle* radar PF 32. This PF was moving towards the radar from east to west. This particular event is annotated in Figure 4.3.

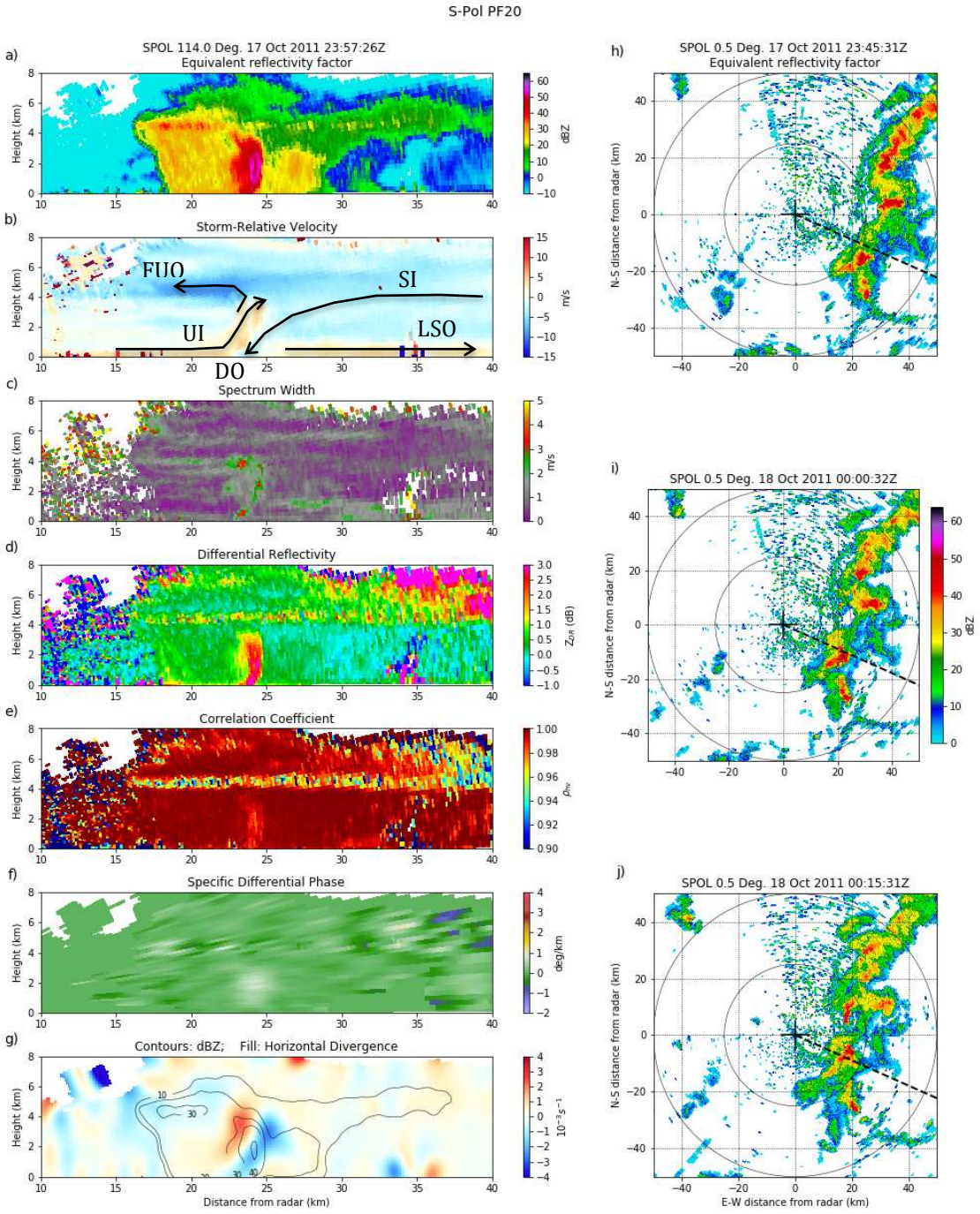

Figure 4.11. Same as Figure 4.10 but showing S-Pol radar PF 95. This PF was moving away from the radar from west to east.

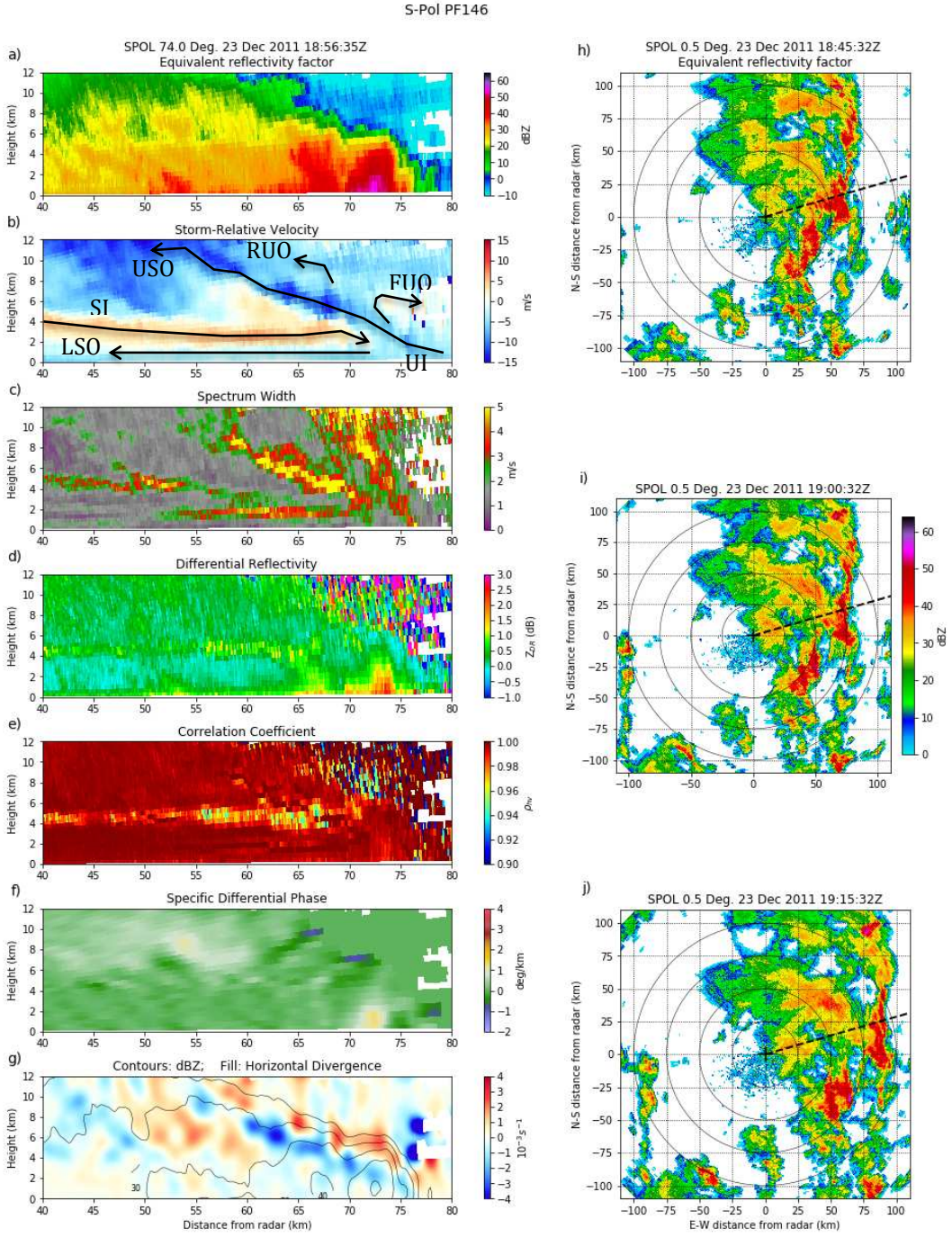

Figure 4.12. Same as Figure 4.5 but showing S-Pol radar PF 146. This PF was moving away from the radar from west to east.

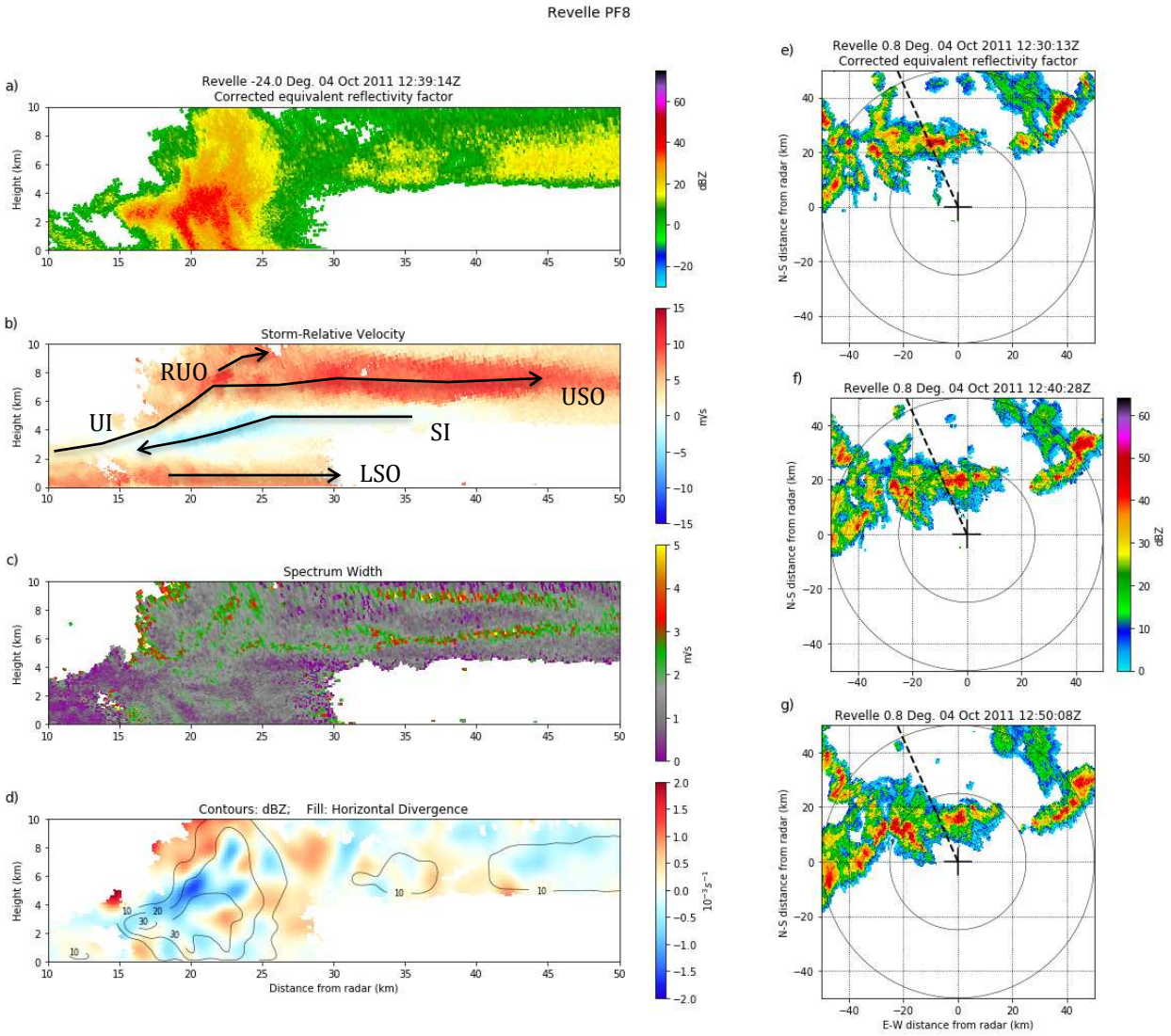

Figure 4.13. Same as Figure 4.4 but showing *Revelle* radar PF 8. This PF was moving towards the radar from NNW to SSE.

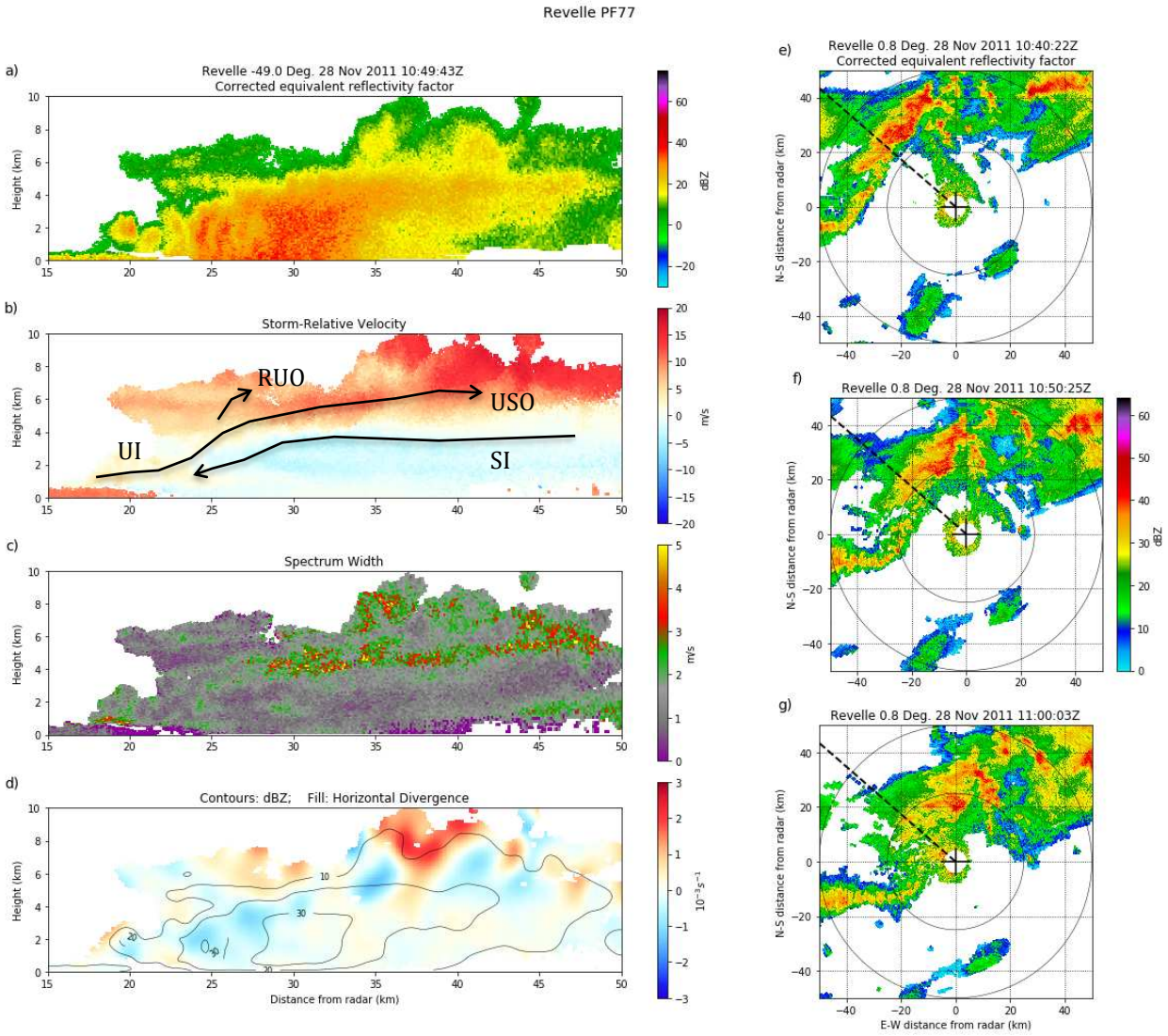

Figure 4.14. Same as Figure 4.4 but showing *Revelle* radar PF 77. This PF was moving towards the radar from NW to SE.

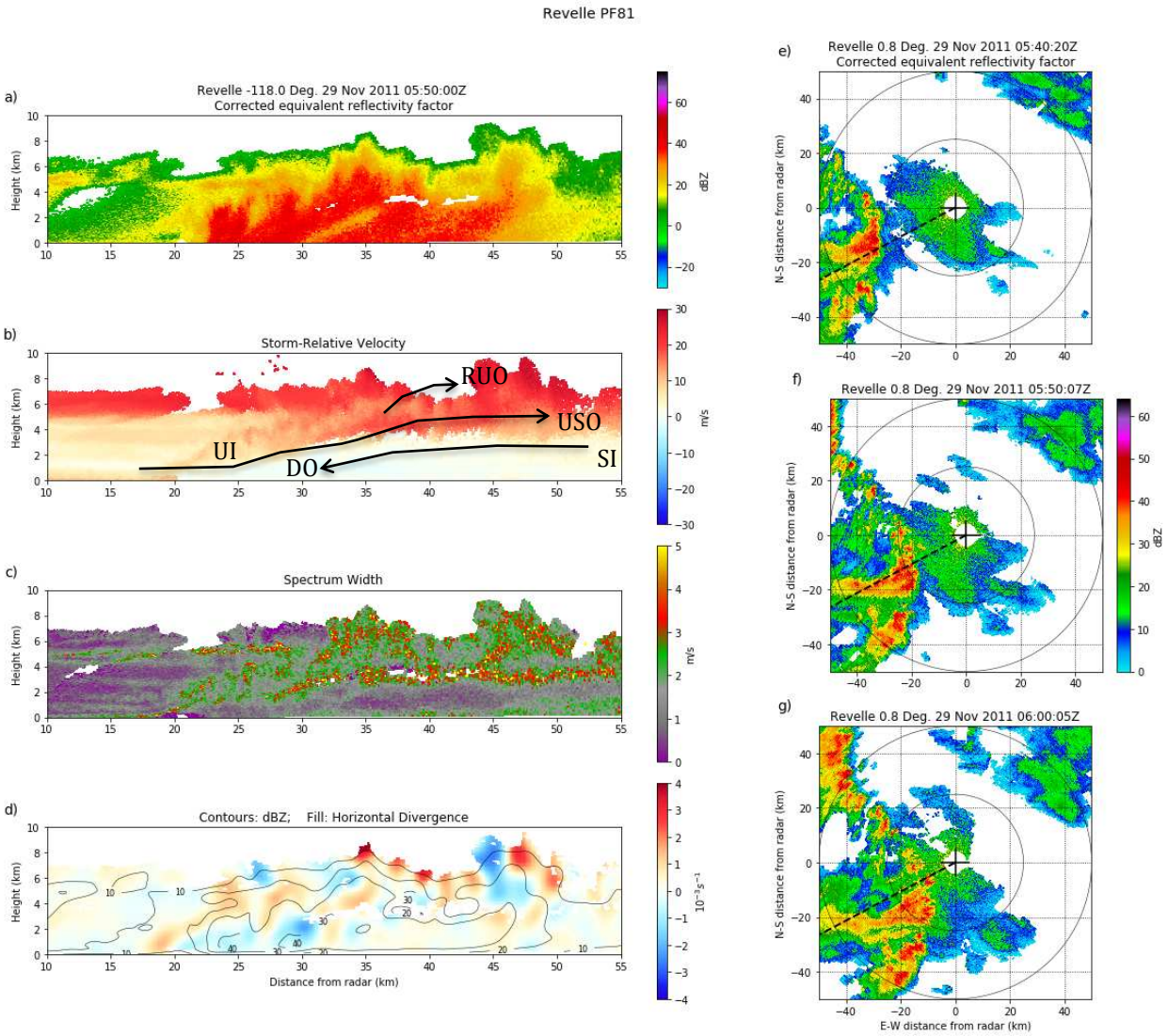

Figure 4.15. Same as Figure 4.4 but showing *Revelle* radar PF 81. This PF was moving towards the radar from WSW to ESE.

CHAPTER 5: CONCLUSION

Mesoscale convective systems (MCSs) have long been known to play a large part in the vertical transport of horizontal momentum (LeMone et al., 1984). They also contribute to the vertical redistribution of heat and radiative forcing owing to extensive cloud cover. Interactions between MCS organization and the Madden-Julian Oscillation (MJO) are not as well understood. In order to shed more light on this problem, we examined the relationship between MCS organization, MCS air flow patterns as a function of the MJO lifecycle, characterized by specific MJO phases.

This study started out by expanding on the works by Alexander and Young (1992), LeMone et al. (1998), Johnson et al. (2005), and Guy and Jorgensen (2014) who examined the relationships between convective organization and shear profiles. These studies were all based on rather limited data samples. Data from the DYNAMO field campaign was examined in detail. Three radars were used to identify linear MCSs providing a significant number of cases to analyze. Soundings taken every three hours were used to diagnose environmental shear. Guy and Jorgensen (2014) found the dominant convective mode of DYNAMO linear features to be parallel to weak low-level (LL) shear. PFs observed during DYNAMO in this study more closely fit the classification of linear convection proposed by LeMone et al. (1998) and Johnson et al. (2005). Specifically, linear features were organized perpendicular to strong LL shear. In the absence of strong LL shear, convective lines were aligned parallel to strong mid-level (ML) shear. When both strong LL and ML shear were present, PFs were aligned perpendicular to LL shear and either parallel to ML shear or had trailing secondary bands that were aligned along the ML shear. One reason our results

were different from those of Guy and Jorgensen (2014) could be that they used flight data from 12.6°S latitude up to the equator and only sampled six events. The sample size we used in our study was substantially larger and our measuring sites were stationary.

The results vary somewhat over the course of the MJO and by location, from the equator to off-equator. The active phases of the MJO (2-3) were more conducive to linear MCS formation both on the equator (S-Pol and *Revelle* radar sites) and off the equator (*Mirai* site). For most systems on the equator, the line orientation was perpendicular to the LL shear. The line orientation and the ML shear were usually parallel. Off the equator, at the R/V *Mirai* location, the relationship was more convoluted. During the active phases of the MJO, the relationship between line orientation and LL shear was similar to that of the equatorial sites (perpendicular to LL shear). There was not a strong correlation between line orientation and ML shear at the *Mirai*. The differences between MCS organization on and off the equator may be attributed to variations in the thermodynamic and synoptic environments. These differences include stronger outgoing longwave radiation anomalies at the equator (Johnson and Ciesielski 2013). Kerns and Chen (2014) indicated that dry air intrusion from the ITCZ inhibited convection over the *Mirai*. Finally, Xu et al. (2015) found there to be less variation of environmental conditions over the course of the MJO south of the equator.

The effects of cold pool strength in linear MCSs was examined and compared to results predicted by RKW theory. These results are broken down by MJO phase to test whether tropical systems in active or inactive MJO phases adhere to RKW theory in a manner similar to those in midlatitudes. Scans from all three DYNAMO radars were used to identify linear MCSs that passed directly over the radar site. Surface meteorological data

was used to identify cold pool strength and, from the cold pool strength, the resulting theoretical density current speed was calculated. The theoretical density current speed did not appear to play a significant role in the propagation speeds of linear systems, as cold pool speeds generally differed from line propagation speeds. This result is consistent with the research of Grant et al. (2018) and, to some extent, Moncrief and Lane (2015). Line propagation speeds are more closely correlated to density current speeds during active MJO phases, but the correlation is only slightly better than during inactive phases.

Finally, vertical cross section (RHI) radar scans were used to study the flow structure within linear MCSs. For the S-Pol radar, polarimetric radar fields were also available, permitting additional insights into couplings between dynamics and microphysics. For the *Revelle* and *Mirai* radars, only reflectivity, Doppler velocity, and spectrum width were available. A storm-relative velocity field was estimated for all features analyzed. Comparisons of our results to those from KH99 and M92 were favorable as five of nine PFs fit both the KH99 and M92 models. Another four PFs fit the M92 model. All events exhibited a jump updraft and descending rear inflow. The presence of these two features support LeMone et al. (1984) and show that these MCSs were transporting front to rear horizontal momentum from low- to mid-levels and rear to front horizontal momentum from mid- to low-levels. Although a descending rear inflow (in the form of a stratiform inflow) was present in all PFs, the absence of a downdraft outflow was not uncommon. This result is consistent with Moncrieff and Lane (2015) and would warrant further investigation before revising the KH99 model. Polarimetric radar fields were useful in this study to identify areas of heavy precipitation associated with areas of high reflectivity in leading convective lines. The Z_{DR} and ρ_{hv} fields provided the location of the melting layer,

and in particular, relations to regions of strong vertical shear caused by interfaces between mesoscale front to rear and rear to front flow. The SW field was also crucial for identifying interfaces between these flows. Multiple rear inflow jets were observed in several PFs. This is another feature that warrants further investigation into its origin and validity for inclusion in future archetypical models.

REFERENCES

Alexander, G.D. and G.S. Young, 1992: The Relationship between EMEX Mesoscale Precipitation Feature Properties and Their Environmental Characteristics. *Mon. Wea. Rev.,* **120**, 554–564.

Balakrishnan, N. and D.S. Zrnic, 1990: Use of Polarization to Characterize Precipitation and Discriminate Large Hail. *J. Atmos. Sci.,* **47**, 1525–1540.

Barnes, G.M. and K. Sieckman, 1984: The Environment of Fast- and Slow-Moving Tropical Mesoscale Convective Cloud Lines. *Mon. Wea. Rev.,* **112**, 1782–1794.

Barnes, H. C., and Houze, R. A., 2014: Precipitation hydrometeor type relative to the mesoscale airflow in mature oceanic deep convection of the Madden-Julian Oscillation, *J. Geophys. Res. Atmos.*, 119,13,990– 14,014.

Bringi, V.N. and V. Chandrasekar, 2001: *Polarimetric Doppler Weather Radar: Principles and Applications*. Cambridge University Press.

Ciesielski, P.E., H. Yu, R.H. Johnson, K. Yoneyama, M. Katsumata, C.N. Long, J. Wang, S.M. Loehrer, K. Young, S.F. Williams, W. Brown, J. Braun, and T. Van Hove, 2014: Quality-Controlled Upper-Air Sounding Dataset for DYNAMO/CINDY/AMIE: Development and Corrections. *J. Atmos. Oceanic Technol.,* **31**, 741–764.

Feng, Z., S. A. McFarlane, C. Schumacher, S. Ellis, J. Comstock, and N. Bharadwaj, 2014: Constructing a merged cloud-precipitation radar dataset for tropical convective clouds during the DYNAMO/AMIE Experiment at Addu Atoll. *J. Atmos. Oceanic Technol.,* **31**, 1021-1042.

Grant, L.D., T.P. Lane, and S.C. van den Heever, 2018: The Role of Cold Pools in Tropical Oceanic Convective Systems. *J. Atmos. Sci.,* **75**, 2615–2634.

Guy, N. and D.P. Jorgensen, 2014: Kinematic and Precipitation Characteristics of Convective Systems Observed by Airborne Doppler Radar during the Life Cycle of a Madden–Julian Oscillation in the Indian Ocean. *Mon. Wea. Rev.,* **142**, 1385–1402.

Helmus, J. J. and Collis, S. M., 2016: The Python ARM Radar Toolkit (Py-ART), a Library for Working with Weather Radar Data in the Python Programming Language. *Journal of Open Research Software*. 4(1), p.e25.

Herzegh, P.H. and A.R. Jameson, 1992: Observing Precipitation through Dual-Polarization Radar Measurements. *Bull. Amer. Meteor. Soc.,* **73**, 1365–1376.

Houze, R. A., 2004: Mesoscale convective systems, *Rev. Geophys*., 42, RG4003.

Houze, R.A., 2014: *Cloud Dynamics (Second Edition)*. Elsevier Inc.

Jameson, A.R., 1985: Microphysical Interpretation of Multiparameter Radar Measurements in Rain. Part III: Interpretation and Measurement of Propagation Differential Phase Shift between Orthogonal Linear Polarizations. *J. Atmos. Sci.,* **42**, 607–614.

Johnson, R.H., S.L. Aves, P.E. Ciesielski, and T.D. Keenan, 2005: Organization of Oceanic Convection during the Onset of the 1998 East Asian Summer Monsoon. *Mon. Wea. Rev.,* **133**, 131–148.

Johnson, R. H., and P. E. Ciesielski, 2013: Structure and properties of Madden–Julian oscillations deduced from DYNAMO sounding arrays. *J. Atmos. Sci.*, **70**, 3157–3179.

Jorgensen, D.P., M.A. LeMone, and S.B. Trier, 1997: Structure and Evolution of the 22 February 1993 TOGA COARE Squall Line: Aircraft Observations of Precipitation, Circulation, and Surface Energy Fluxes. *J. Atmos. Sci.,* **54**, 1961–1985.

Katsumata, M., T. Ushiyama, K. Yoneyama, and Y. Fujiyoshi, 2008: Combined use of TRMM/PR and disdrometer data to correct reflectivity of ground-based radars. *SOLA*, **4**, 101–104.

Keenan, T. D., and R. E. Carbone, 1992: A preliminary morphology of precipitation systems in tropical northern Australia. *Quart. J. Roy. Meteor. Soc.*, **118**, 283–326.

Kerns, B.W. and S.S. Chen, 2014: Equatorial Dry Air Intrusion and Related Synoptic Variability in MJO Initiation during DYNAMO. *Mon. Wea. Rev.,* **142**, 1326–1343.

Kingsmill, D. E. and Houze, R. A., 1999: Kinematic characteristics of air flowing into and out of precipitating convection over the west Pacific warm pool: An airborne Doppler radar survey. *Q.J.R. Meteorol. Soc*., 125: 1165-1207.

Lane, T. P., and M. W. Moncrieff, 2015: Long-lived mesoscale systems in a low–convective inhibition environment. Part I: Upshear propagation. *J. Atmos. Sci.*, **72**, 4297–4318.

LeMone, M.A., 1983: Momentum Transport by a Line of Cumulonimbus. *J. Atmos. Sci.,* **40**, 1815–1834.

LeMone, M.A., G.M. Barnes, and E.J. Zipser, 1984: Momentum Flux by Lines of Cumulonimbus over the Tropical Oceans. *J. Atmos. Sci.,* **41**, 1914–1932.

LeMone, M.A., E.J. Zipser, and S.B. Trier, 1998: The Role of Environmental Shear and Thermodynamic Conditions in Determining the Structure and Evolution of Mesoscale Convective Systems during TOGA COARE. *J. Atmos. Sci.,* **55**, 3493–3518.

Madden, R.A. and P.R. Julian, 1971: Detection of a 40–50 Day Oscillation in the Zonal Wind in the Tropical Pacific. *J. Atmos. Sci.,* **28**, 702–708.

Madden, R.A. and P.R. Julian, 1972: Description of Global-Scale Circulation Cells in the Tropics with a 40–50 Day Period. *J. Atmos. Sci.,* **29**, 1109–1123.

Markowski, P. and Y. Richardson, 2010: *Mesoscale Meteorology in Midlatitudes*. John Wiley and Sons.

Moncrieff, M. W., 1992: Organized Convective Systems: Archetypal Dynamical Models, Mass and Momentum Flux Theory, and Parametrization. *Q.J.R. Meteorol. Soc*., 118: 819-850.

Moncrieff, M.W. and T.P. Lane, 2015: Long-Lived Mesoscale Systems in a Low–Convective Inhibition Environment. Part II: Downshear Propagation. *J. Atmos. Sci.,* **72**,4319–4336.

Parker, M.D. and R.H. Johnson, 2004: Structures and Dynamics of Quasi-2D Mesoscale Convective Systems. *J. Atmos. Sci.,* **61**, 545–567.

Rickenbach, T.M. and S.A. Rutledge, 1998: Convection in TOGA COARE: Horizontal Scale, Morphology, and Rainfall Production. *J. Atmos. Sci.,* **55**, 2715–2729.

Rotunno, R., J. B. Klemp, and M. L. Weisman, 1988: A theory for strong, long-lived squall lines. *J. Atmos. Sci.*, **45**, 463–485.

Rutledge, S.A. and R.A. Houze, 1987: A Diagnostic Modeling Study of the Trailing Stratiform Region of a Midlatitude Squall Line. *J. Atmos. Sci.,* **44**, 2640–2656.

Simpson, J., R.F. Adler, and G.R. North, 1988: A Proposed Tropical Rainfall Measuring Mission (TRMM) Satellite. *Bull. Amer. Meteor. Soc.,* **69**, 278–295.

Smull, B.F. and R.A. Houze, 1985: A Midlatitude Squall Line with a Trailing Region of Stratiform Rain: Radar and Satellite Observations. *Mon. Wea. Rev.,* **113**, 117–133.

Thompson, E.J., S.A. Rutledge, B. Dolan, M. Thurai, and V. Chandrasekar, 2018: Dual-Polarization Radar Rainfall Estimation over Tropical Oceans. *J. Appl. Meteor. Climatol.,* **57**, 755–775.

UCAR/NCAR - Earth Observing Laboratory. 2016. R/V Roger Revelle ISS Surface Meteorology Data. Version 1.0. UCAR/NCAR - Earth Observing Laboratory. https://doi.org/10.5065/D6GB22F4. Accessed 07 Jan 2019.

Weisman, M. L., and R. Rotunno, 2004: "A theory for strong long-lived squall lines" revisited. *J. Atmos. Sci.*, **61**, 361–382.

Wheeler, M. and H. H. Hendon, 2004: An all-season real-time multivariate MJO index: Development of an index for monitoring and prediction. *Mon. Wea. Rev.*, **132**, 1917–1932.

Xu, W. and S.A. Rutledge, 2014: Convective Characteristics of the Madden–Julian Oscillation over the Central Indian Ocean Observed by Shipborne Radar during DYNAMO. *J. Atmos. Sci.,* **71**, 2859–2877.

Xu, W. and S. A. Rutledge, 2015: Morphology, intensity, and rainfall production of MJO convection: Observations from DYNAMO shipborne radar and TRMM. *J. Atmos. Sci.*, **72**, 623–640.

Xu, W., S.A. Rutledge, C. Schumacher, and M. Katsumata, 2015: Evolution, Properties, and Spatial Variability of MJO Convection near and off the Equator during DYNAMO. *J. Atmos. Sci.,* **72**, 4126–4147.

Yoneyama, K., C. Zhang, and C.N. Long, 2013: Tracking Pulses of the Madden–Julian Oscillation. *Bull. Amer. Meteor. Soc.,* **94**, 1871–1891.

Zhang, C., 2005: Madden-Julian Oscillation, *Rev. Geophys.*, 43, RG2003.

Zuluaga, M.D. and R.A. Houze, 2013: Evolution of the Population of Precipitating Convective Systems over the Equatorial Indian Ocean in Active Phases of the Madden–Julian Oscillation. *J. Atmos. Sci.,* **70**, 2713–2725.